HHS Public Access

Author manuscript

Cell Rep. Author manuscript; available in PMC 2022 August 14.

Published in final edited form as:

Cell Rep. 2022 July 19; 40(3): 111085. doi:10.1016/j.celrep.2022.111085.

Synaptic hyperexcitability of cytomegalic pyramidal neurons contributes to epileptogenesis in tuberous sclerosis complex

Xiaoping Wu[1,9], **Alexander A. Sosunov**[1,9], **Wudu Lado**[2], **Jia Jie Teoh**[3], **Ahrom Ham**[2], **Hongyu Li**[2], **Osama Al-Dalahmah**[4], **Brian J.A. Gill**[1], **Ottavio Arancio**[4,7,8], **Catherine A. Schevon**[2], **Wayne N. Frankel**[3], **Guy M. McKhann II**[1], **David Sulzer**[5,6], **James E. Goldman**[4,8], **Guomei Tang**[2,10,*]

[1]Department of Neurological Surgery, Columbia University Irving Medical Center, New York, NY 10032, USA

[2]Department of Neurology, Columbia University Irving Medical Center, New York, NY 10032, USA

[3]Institute for Genomic Medicine, Columbia University Irving Medical Center, New York, NY 10032, USA

[4]Department of Pathology and Cell Biology, Columbia University Irving Medical Center, New York, NY 10032, USA

[5]Department of Psychiatry, Columbia University Irving Medical Center, New York, NY 10032, USA

[6]Department of Pharmacology, Columbia University Irving Medical Center, New York, NY 10032, USA

[7]Department of Medicine, Columbia University Irving Medical Center, New York, NY 10032, USA

[8]The Taub Institute, Columbia University Irving Medical Center, New York, NY 10032, USA

[9]These authors contributed equally

[10]Lead contact

SUMMARY

Tuberous sclerosis complex (TSC) is a developmental disorder associated with epilepsy, autism, and cognitive impairment. Despite inactivating mutations in the *TSC1* or *TSC2* genes and hyperactive mechanistic target of rapamycin (mTOR) signaling, the mechanisms underlying TSC-associated neurological symptoms remain incompletely understood. Here we generate a *Tsc1*

*Correspondence: gt2107@cumc.columbia.edu.

AUTHOR CONTRIBUTIONS

G.T. and J.E.G. designed the project and wrote the paper. A.H., H.L., and G.T. performed mouse breeding and behavioral analysis. X.W., A.A.S., W.L., and G.T. conducted electrophysiological, histological, and biochemical analyses. X.W., B.J.A.G., and C.A.S. performed multi-electrode array analysis. J.J.T. and W.N.F. performed video-EEG analysis. G.T. and O.A.-D. performed RNA-seq analysis. X.W., A.A.S., O.A.-D., B.J.A.G., and G.T. analyzed the data. D.S., G.M.M., and O.A. consulted on electrophysiology experimental design and analysis. All authors provided critical feedback and helped shape the research, analyses, and manuscript.

SUPPLEMENTAL INFORMATION

Supplemental information can be found online at https://doi.org/10.1016/j.celrep.2022.111085.

DECLARATION OF INTERESTS

The authors declare no competing interests.

conditional knockout (CKO) mouse model in which *Tsc1* inactivation in late embryonic radial glia causes social and cognitive impairment and spontaneous seizures. *Tsc1* depletion occurs in a subset of layer 2/3 cortical pyramidal neurons, leading to development of cytomegalic pyramidal neurons (CPNs) that mimic dysplastic neurons in human TSC, featuring abnormal dendritic and axonal overgrowth, enhanced glutamatergic synaptic transmission, and increased susceptibility to seizure-like activities. We provide evidence that enhanced synaptic excitation in CPNs contributes to cortical hyperexcitability and epileptogenesis. In contrast, astrocytic regulation of synapse formation and synaptic transmission remains unchanged after late embryonic radial glial *Tsc1* inactivation, and astrogliosis evolves secondary to seizures.

Graphical Abstract

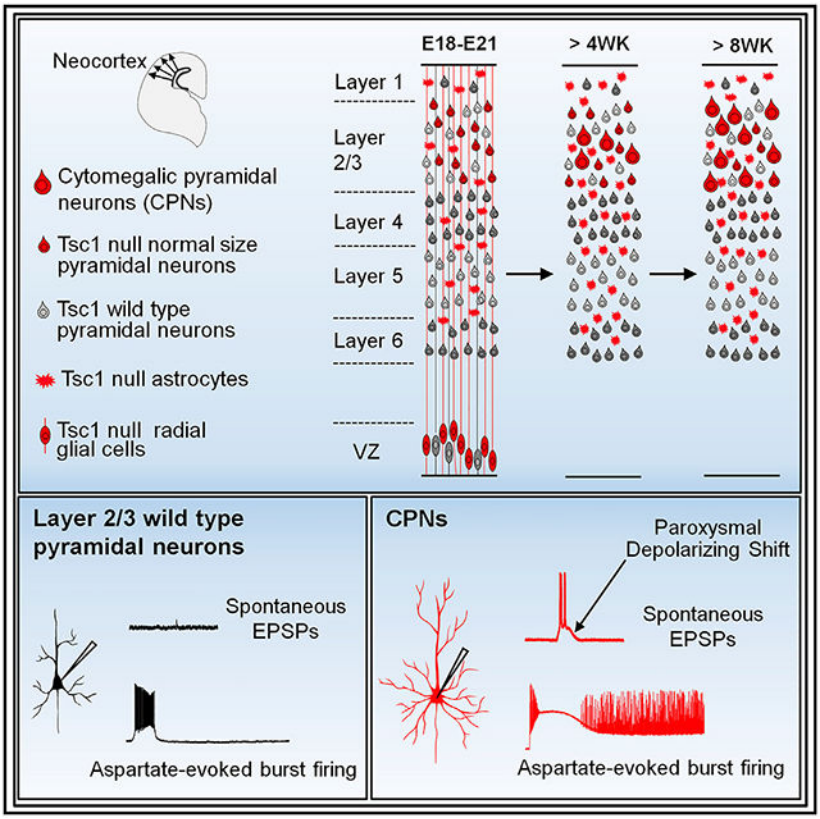

In brief

Wu et al. demonstrate that Tsc1 inactivation in late embryonic radial glial cells (RGCs) produces cytomegalic pyramidal neurons that mimic TSC-like dysplastic neurons. They find that enhanced excitatory synaptic transmission in Tsc1-null cytomegalic pyramidal neurons contributes to cortical hyperexcitability and epileptogenesis.

INTRODUCTION

Tuberous sclerosis complex (TSC) is an autosomal dominant disorder caused by inactivating mutations in *TSC1* or *TSC2*, leading to hyperactivation of mechanistic target of rapamycin

(mTOR) signaling (Curatolo and Maria, 2013; Sahin et al., 2016). Individuals with TSC suffer from a wide spectrum of neurological symptoms, including seizures, autism, cognitive disability, and neurobehavioral deficits. The mechanisms underlying this clinical variability are not fully understood but may involve the numbers and locations of cortical tubers (Goodman et al., 1997; Bolton and Griffiths, 1997; Bolton et al., 2015), the characteristic brain pathology of TSC that features cortical dyslamination, and cellular abnormalities, including reactive astrocytes, cytomegalic dysplastic neurons, and giant cells (Crino, 2013).

Development of TSC cellular pathology is thought to be associated with genetic and environmental factors that affect the temporal and spatial distribution of "second hit" somatic mutations, leading to genetic mosaicism caused by complete inactivation of *TSC1/2* in embryonic neuroprogenitor cells (Crino, 2013; Goto et al., 2011). In mouse models, biallelic *Tsc1/2* inactivation in early embryonic neuroprogenitor cells (NPCs), such as neuroepithelial precursors (NEPs) at embryonic day 9.5 (E9.5) (Emx-1 Cre), neural stem cells at E12.5 (Nestin-Cre), and radial glial cells (RGCs) (hGFAP2-Cre) at E13.5, recapitulates tuber-like cellular pathology with enlarged neurons, abnormal myelination, astrocyte gliosis, and cortical dyslamination (Magri et al., 2011, 2013; Carson et al., 2012; Anderl et al., 2011; Goto et al., 2011; Uhlmann et al., 2002; Way et al., 2009; Mietzsch et al., 2013). The multilineage potential of early NPCs (Desai and McConnell, 2000), together with early onset of seizures and early lethality in these models, prevented these studies from examining the role of specific cell types in TSC pathogenesis. *In utero* electroporation (IUE) models with somatic *Tsc1/2* deletion, via CRISPR-Cas9 genome editing at E14 (Lim et al., 2017; Goz et al., 2020) or Cre-mediated single-cell *Tsc1* knockout at E15 (Feliciano et al., 2011), often develop tuber-like focal lesions featuring cortical dyslamination and cytomegalic pyramidal neurons and increased susceptibility to seizures, supporting a role of *Tsc1*-null cytomegalic neurons in seizure initiation, but it remains incompletely known how these neurons contribute to epileptogenesis.

This study aims to further our understanding of the role of cytomegalic pyramidal neurons in TSC-related neurological symptoms. We have generated a *Tsc1* conditional knockout mouse model using the mouse glial fibrillary acidic protein (Gfap) promoter-driven Cre (*mGfap*-Cre) recombinase (Garcia et al., 2004). Cre-mediated recombination begins in cortical and hippocampal RGCs at E18, leading to *Tsc1* inactivation in a subset of layer 2/3 upper cortical and hippocampal pyramidal neurons and the vast majority of astrocytes. The resulting $Tsc1^{mGfap\text{-}Cre}$ conditional knockout (CKO) mice show social and cognitive impairment at postnatal weeks 4–5 and spontaneous seizures after postnatal week 8. Many, but not all, *Tsc1*-null pyramidal neurons become cytomegalic, showing increased mTOR activity, enlarged somata, dendritic and axonal overgrowth, enhanced excitatory synaptic transmission, and increased susceptibility to seizure-like activities. In contrast, astrocyte functions that regulate synapse formation and synaptic transmission, including astrocyte glutamate uptake, potassium buffering, and astrocyte-regulated synaptogenesis, remain unaltered prior to first-time seizures, and astrogliosis occurs until after the onset of first seizures. Our data support the hypothesis that late embryonic RGC loss of *Tsc1* causes cortical hyperexcitability and epilepsy through enhanced synaptic excitation in cytomegalic pyramidal neurons.

RESULTS

mGfap-Cre-mediated recombination in late embryonic RGCs

To determine the timing and cell type specificity of *mGfap-Cre*-mediated recombination, we crossed *mGfap-Cre* mice with *Ai9* Cre-reporter mice in which the expression of tdTomato (tdT) is induced upon Cre expression. In the resulting *mGfap-Cre:Ai9+* mice, tdT expression began at E18 (Figure 1A) in 12.7% (76 of 597) of cortical and hippocampal RGCs (Figure 1B). At this age, some tdT+ cells were newborn neurons positive for the neuronal marker Tuj1 (Figure 1C).

The progeny of cortical and hippocampal RGCs (i.e., neurons and astrocytes) were examined at postnatal week 4. Nearly all (>99%, 443 of 447) glutamine synthetase (GS)/S100β-positive cortical (Figure 1D) and hippocampal (data not shown) astrocytes showed recombination. About 7% (217 of 3,167) of NeuN (neuronal nuclei) positive (NeuN+) neurons in the retrosplenial, visual and somatosensory cortices expressed tdT. The majority of tdT+ neurons were layer 2/3 pyramidal neurons, accounting for ~20% (301 of 1,493) of NeuN+ neurons in the upper cortex. In the hippocampus, tdT+ neurons were found in the cornu ammonis (CA) areas (~6%, 198 of 3,367 NeuN+ cells) and the dentate gyrus (DG) granule layer (~40%, 345 of 896 NeuN+ cells) (Figures 1E and 1F). We confirmed this neuronal recombination using *ROSA26R-EYFP* (Srinivas et al., 2001) and RiboTag (Sanz et al., 2009) Cre reporter mice (Figures S1A and S1B).

Tsc1 inactivation in late embryonic RGCs causes TSC-related neurological symptoms

By crossing $Tsc1^{flox/flox}$ mice to *mGfap*-Cre and *Ai9+* mice, we generated *Tsc1CKO:Ai9+* (CKO) mice that express tdT in *Tsc1* KO (*Tsc1*KO) cells. Similar to *mGfap*-Cre+:Ai9+ controls (CTRLs), CKO mice showed recombination in more than 99% of astrocytes and ~7% of neurons in the retrosplenial, visual, and somatosensory cortical regions (data not shown). Loss of Tsc1 protein and the resulting mTOR hyperactivation were detected in some tdT+ cells starting from E20 (Figure S1C), coincident with the long half-life (~22 h) of residual cytoplasmic wild-type (WT) Tsc1 protein (Lee et al., 2007). *Tsc1* inactivation was also evidenced by enhanced mTOR activity at different ages, indicated by increased levels of phosphorylated mTOR (p-mTOR) and S6 (p-S6) (Figures S2A and S2B).

All CKO mice survived during the first 12 postnatal weeks (Figure 2A, left), with ~28% showing spontaneous, recurrent seizures at the beginning of postnatal week 9 and 38% with seizures at postnatal weeks 11–12 (Figure 2A, right). By postnatal week 15, ~45% of CKO mice had seizures, and ~30% of these had died. By postnatal week 28, ~67% of CKO mice had seizures, and ~50% of them had died. Seizure behavior varied in form and severity, ranging from myoclonic seizures with frequent jerking of the head and body and chewing to tonic-clonic convulsive seizures with extension of fore- or hindlimbs, falling on one side, and rearing and bouncing in the home cage (Figure 2B; Videos S1 and S2). The episodes lasted for 0.5–2 min and were followed by physical inactivity before complete recovery. Behavioral seizures and seizure incidence were confirmed by video electroencephalogram (EEG) recording (Figure 2C).

TSC-related neuropsychiatric symptoms were evaluated at postnatal weeks 4–5, when seizures were absent. Compared with CTRL littermates, CKO mice showed normal locomotor and anxiety-like behaviors in the open field test and normal motor coordination during the testing session of the rotarod test but spent more time self-grooming, a behavior thought to indicate autism-like repetitive behaviors (Figures S2C-S2I). CKO mice also exhibited reduced preferences for social targets and social novelty (Figures 2D-2F), impaired early-phase motor skill learning (Figure S2I), impaired novel object recognition (Figure 2G), and contextual fear memory (Figure 2H).

Tsc1 inactivation in late embryonic RGCs produces cytomegalic pyramidal neurons

Many, but not all, tdT+ layer 2/3 upper cortical pyramidal neurons in CKO mice showed hyperactive mTOR, indicated by increased levels of p-S6 and p-mTOR (Figures 3A-3C). Further analysis indicated that all upper cortical pyramidal neurons from *mGfap*-Cre:Ai9+ (CTRL) mice (referred to as *Tsc1*WT neurons), including tdT− and tdT+ neurons, had similar somal diameters ranging from 10–18 μm at postnatal weeks 4 (Figures 3D) and 15 (data not shown). In CKO mice, tdT− upper cortical pyramidal neurons had normal somal diameters of 10–18 μm. In contrast, tdT+ pyramidal neurons showed somal diameters over a wide range: some were of “normal size” within the range of *Tsc1*WT neurons, whereas many others displayed enlarged somal diameters greater than 20 μm. With age, significantly more tdT+ neurons became enlarged (Figure 3D). By postnatal week 24, many tdT+ neurons had diameters 2- to 3-fold greater than those of *Tsc1*WT neurons.

To confirm Cre-mediated depletion of *Tsc1*, we extracted nuclei from distinct tdT− and tdT+ upper cortical pyramidal neurons from CKO mice using patch-clamp pipettes and genotyped for conditional floxed and null alleles of Tsc1, as in Meikle et al. (2005). Normal-sized and enlarged tdT+ neurons showed one single band for the null *Tsc1* allele, indicative of *Tsc1* loss. In contrast, tdT− upper cortical pyramidal neurons did not undergo recombination, showing one single band for the floxed *Tsc1* allele (Figure 3E).

The enlarged tdT+ *Tsc1*KO upper cortical pyramidal neurons, to which we refer as cytomegalic pyramidal neurons (CPNs), resembled the dysplastic neurons in human TSC (Cepeda et al., 2010; Sosunov et al., 2015) in that they showed mTOR hyperactivation (Figures 3A-3C), enlarged somal size (Figure 3D), enlarged nuclei (mean diameter ± SEM: 16.4 ± 0.5 μm in CPNs and 9.8 ± 0.3 μm in *Tsc1*WT neurons, $p < 0.001$, unpaired t test), increased levels of NMDA (N-methyl-D-aspartate) receptors (NMDAR) and AMPA (α-amino-3-hydroxy-5-methyl-4-isoxazole propionic acid) receptors (AMPAR) (Figures 3F-3H), somatic accumulation of neurofilament (NFT) protein, and lack of immunoreactivity to typical markers for inhibitory neurons (parvalbumin [PV], glutamic-acid decarboxylase [GAD 65/67], and gamma-aminobutyric acid [GABA]) and giant cells (vimentin [Vim] and GS) (Figures S3).

In contrast, normal-sized tdT+ *Tsc1*KO neurons expressed levels of p-S6 and p-mTOR similar to those of adjacent tdT− upper cortical pyramidal neurons (Figures 3A-3C). Like CPNs, these neurons showed pyramid-shaped somata, apical and basal dendrites, and dendritic spines (Figures 5A and 5C) but no expression of inhibitory neuronal markers

(Figures S3). The presence of normal-sized *Tsc1*KO pyramidal neurons was confirmed in CKO mice expressing the RiboTag Cre reporter (Figure S1D).

tdT+ DG granule neurons from CKO and CTRL mice were also comparable in p-S6 levels and somal diameters (Figure S4A). When immunostaining for Znt3 (Figures S4B and S4C), an axonal marker of granule neurons (Pun et al., 2012), we did not find mossy fiber sprouting, a typical feature of temporal lobe epilepsy characterized by axonal outgrowth of granule neurons that project to their own dendritic fields in the inner molecular layer (Sutula et al., 1989; Buckmaster and Lew, 2011). The lack of morphological changes of DG granule neurons in response to *Tsc1* inactivation suggests a neuronal type-specific effect of *Tsc1* inactivation on cytomegaly.

Tsc1 inactivation in late embryonic RGCs has no effects on cortical lamination

Because cortical dyslamination is a prominent feature in human TSC (Crino, 2013), we asked whether formation of cortical layers was disrupted in CKO mice. By immunostaining for the layer-specific markers Cux1 (layers 2–4) and Ctip2 and Foxp2 (layers 5–6), we found no obvious defects in cortical layering in CKO mice (Figure S5A), and there were no changes in cortical thickness (Figure S5B). Occasionally, Ctip2−/Cux1+/tdT+ pyramidal neurons can be seen in the lower cortex (Figure S5C), suggesting a defect in neuronal migration. These data indicate that *Tsc1* deletion in E18 RGCs could not produce sufficient CPNs to interfere with cortical lamination.

Tsc1 inactivation in late embryonic RGCs does not affect astrocyte functions

Astrocyte gliosis and dysfunction, manifested by increased Gfap levels, decreased levels of glutamate transporter-1 (GLT1) and glutamate aspartate transporter (GLAST), and impaired astrocyte glutamate uptake, have been implicated in epileptogenesis of TSC (Uhlmann et al., 2002; Wong et al., 2003; Jansen et al., 2005; Wong, 2019). Given that most astrocytes in our mice showed recombination, we characterized *Tsc1*-null astrocytes at different ages.

In CKO mice at postnatal week 4, when seizures were absent, we found no changes in astrocyte Gfap or GLT1 immunofluorescence (Figure 4A). Western blot analysis of the upper cortex revealed a subtle increase in Gfap protein levels (Figure S6A), which may reflect changes in very few astrocytes (Figure 4A), and we did not find significant increases in the abundance of *Gfap* transcripts (Figure S6B). Although transcription of the *Vim* and *Thbs4* genes was upregulated, there were no changes at Vim and TSP4 protein levels (Figures S6A and S6B). More importantly, most key proteins implicated in basic astrocyte functions (Chung et al., 2015) remained unaltered at postnatal weeks 4 and 8 (Figure S6A), including astrocyte glutamate uptake (GLT1 and GLAST), astrocyte potassium (K^+) buffering (inward rectifier K^+ channel Kir4.1), astrocyte water uptake (aquaporin 4 [AQP4]), astrocyte coupling (Connexin 43), glutamate/glutamine homeostasis and ammonia detoxification (GS), and astrocyte-regulated synaptogenesis (glypican, SPARCL1/hevin, thrombospondins TSP1/2 and TSP4, and tyrosine-protein kinase Mer [MertK]).

After postnatal week 15, CKO mice without seizures showed normal levels of Gfap and GLT1 (Figure 4B). However, in mice that had seizures, a majority of *Tsc1*KO astrocytes exhibited an increase in Gfap fluorescence, indicative of astrocytic gliosis, accompanied

by a reduction in GLT1 levels in some astrocytes (Figure 4B). Mice with seizures showed transcriptional upregulation of reactive astrocyte genes, including *Gfap, Vim, Serpina3n, CXCL10, CD44*, and many others (Figure S6C), and an increase in Gfap and Vim but a reduction in GLT1 and GLAST at the protein level (Figure S6A).

We noted that the number of CPNs varied between individual CKO mice after postnatal week 15 (Figure 4C), with significantly more in mice with seizures than in those without. Further analysis revealed a positive correlation between the level of Gfap and the number of CPNs in CKO mice (Figures 4C and 4D) and that significantly more astrocytes had higher p-S6 levels (Figures 4C and 4E) in mice with seizures than those without. These results suggest that seizures, in association with the increased number of CPNs, may exacerbate astrocyte mTOR hyperactivation and induce astrogliosis throughout the cortex.

Using whole-cell patch-clamp recordings, we assessed astrocyte glutamate uptake and K^+ buffering, two essential functions by which astrocytes regulate glutamatergic synaptic transmission through uptake of excessive glutamate and K^+ from the synaptic cleft. The glutamate transporter-mediated inward current was induced by puff application of 1 mM D-aspartic acid (Asp) (Glowatzki et al., 2006; Rimmele et al., 2017), and potassium uptake capacity was assessed by focal application of 30 mM potassium chloride (KCl) (Sosunov et al., 2013). CKO mice without seizures showed normal capacity for astrocyte glutamate and K^+ uptake at postnatal weeks 4 and 15 (Figures 4F-4I). *Tsc1*-null astrocytes, however, exhibited an increase in membrane capacitance and a reduction in membrane input resistance (Table S1), indicative of a larger astrocyte cell size.

The lack of astrogliosis and astrocyte dysfunction was confirmed in an inducible *Tsc1*$^{hGFAP\text{-}CreER}$CKO:Ai9+ mouse model mediated by the human glial fibrillary acidic protein (hGFAP) promoter-driven CreER^{T2} (*hGFAP-Cre*ER) (Ganat et al., 2006). CreER expression was induced by tamoxifen at post-natal day 14 (P14), P16, and P18, resulting in recombination in ~80% of upper cortical astrocytes (Figure S6D), less than 0.5% of cortical pyramidal neurons (3 tdT+ out of 1,650 NeuN+ cortical neurons), and adult neuroprecursors in subventricular and subgranular zones (data not shown). Tamoxifen-induced *Tsc1*$^{hGFAP\text{-}CreER}$CKO:Ai9+ mice did not show behavioral seizures (0 of 16 mice) or a reduction in glutamate uptake in tdT+ astrocytes after postnatal week 16 (Figure S6E). In the upper cortex, tdT+ *Tsc1*KO astrocytes were similar to adjacent tdT− *Tsc1*WT astrocytes in levels of Gfap, GS, GLT-1, and p-S6 (Figure S6F).

CPNs exhibit enhanced glutamatergic synaptic transmission with intact inhibitory synaptic input

Our data suggest that *Tsc1* inactivation by itself is insufficient to compromise astrocyte function and that astrocyte gliosis evolves secondary to seizures. These findings suggest that CPNs could be a major contributing factor to epileptogenesis. To address this possibility, we characterized the anatomical and electrophysiological properties of tdT− and tdT+ layer 2/3 upper cortical pyramidal neurons in the somatosensory cortex (SSC)/retrosplenial cortex (RSC) of *mGfap-Cre:Ai9+* (CTRL) and CKO mice at different ages prior to onset of seizures (postnatal week 4 or 8) or after postnatal week 15 in mice that had developed seizures.

We previously showed a link between excessive dendrite spines and autism-like social impairment (Tang et al., 2014), and, thus, we examined basal dendritic spine density at postnatal weeks 4–5 (Figures 5A and 5B), the age when CKO mice showed social and cognitive deficits. No differences were found between tdT+ and tdT− *Tsc1*WT neurons in *mGfap-Cre:Ai9+* CTRL mice. In CKO mice, CPNs had a significantly higher spine density than tdT− and normal-sized *Tsc1*KO neurons, and the latter two neuronal types showed spine densities similar to tdT+ or tdT− *Tsc1*WT neurons from CTRL mice.

Dendritic tree morphology was assessed using intracellular Lucifer yellow injection. tdT− and tdT+ normal-sized neurons from CKO mice had dendritic architecture similar to that in tdT− or tdT+ *Tsc1*WT neurons from CTRL mice. CPNs, however, showed an increase in dendritic tree complexity at postnatal weeks 4 and 15, as indicated by increased primary dendritic ramification (Figures 5C-5E) and exuberant, thin, undulating processes emanating from all regions of the soma (Figure 5F). The axons of CPNs branched extensively, with retrograde collaterals curving back toward the apical dendrites (Figure 5G).

By whole-cell patch-clamping, we observed abnormal membrane properties in CPNs. At all ages, compared with other neuronal types, CPNs showed similar resting membrane potential (RMP) but a reduction in membrane resistance and an increase in capacitance (Figure 5H and Table S2), whereas tdT− and tdT+ normal-sized neurons from CKO mice had membrane properties comparable with *Tsc1*WT neurons from CTRL mice. We noted a reduction in action potential (AP) firing in response to current injection in CPNs (Figure 5I), but there were no changes in AP threshold, AP height, or AP duration despite AP latency being longer in CPNs (Table S3).

We next compared spontaneous excitatory postsynaptic currents (sEPSCs) between different neuronal types. At postnatal week 4, CPNs showed an increase in sEPSC frequency but no differences in amplitude from other neuronal types (Figure 5J). At postnatal week 8, sEPSC frequency in CPNs was similar to other neuronal types, but the amplitude became significantly larger (Figure 5K). By postnatal week 15, CPNs continued to show a higher sEPSC amplitude (Figure 5L) but with slower rise and decay time courses (Table S4).

Similar changes were observed for miniature EPSCs (mEPSCs) in CPNs. At postnatal week 4, CPNs showed a significantly higher mEPSC frequency but no changes in mEPSC amplitude (Figure S7A), consistent with increased dendritic spine density. After postnatal week 8, mEPSC amplitude increased, whereas frequency became normal in CPNs (Figure S7B). The increase in excitatory synaptic activities was not accompanied by synaptic disinhibition, as indicated by similar amplitude and frequency of spontaneous inhibitory postsynaptic currents (IPSCs) between CPNs and tdT+ *Tsc1*WT neurons from CTRL mice (Figure S7C).

Our data demonstrate a cell-autonomous effect of *Tsc1* inactivation on enhanced excitatory synaptic transmission in CPNs. tdT− upper cortical pyramidal neurons were surrounded by *Tsc1*WT astrocytes in *mGfap-Cre:Ai9+* CTRLs but by *Tsc1*KO astrocytes in CKO mice. However, the anatomical and synaptic properties of tdT− neurons and the levels of astrocyte-secreted synaptogenic proteins (e.g., glypican, hevin, thrombospondins, and MERTK) were

similar between CTRL and CKO mice (Figure S6A), suggesting that *Tsc1*-null astrocytes play a normal role in regulating synapse formation and synaptic function in our CKO mice.

CPNs are more susceptible to NMDAR-mediated epileptiform activities

In voltage-clamp mode, in addition to typical EPSCs, we observed spontaneous giant inward currents of large amplitude (>150 pA) and long duration (>100 ms) in CPNs after postnatal week 8, with a frequency of 0.044 ± 0.021 Hz. The giant inward currents were not seen in tdT+ *Tsc1*WT neurons from CTRL mice and were identified in current-clamp mode as frequent APs riding on a giant depolarizing potential (Figure 6A). These events resembled paroxysmal depolarization shift (PDS), a cellular correlate of electrographic interictal spikes (Hotka and Kubista, 2019) that is thought to be initiated by a network-driven giant EPSP triggered by AMPAR-mediated fast transmission and sustained by prolonged NMDAR-mediated EPSPs (Stafstrom, 2010). The spontaneous PDS-like events were blocked by the sodium channel blocker tetrodotoxin (TTX) or MK-801 (Figure 6B), an NMDAR open channel blocker that use-dependently blocks active synaptic NMDARs (Huettner and Bean, 1988; Tovar and Westbrook, 2002; Liu et al., 2007; Atasoy et al., 2008; Sun et al., 2017).

We next asked whether AMPAR- and NMDAR-mediated synaptic transmission were altered in CPNs. By measuring electrically evoked EPSCs (eEPSCs), we found no differences in AMPA or NMDA eEPSCs at postnatal week 4 (Figure 6C). After postnatal week 8, CPNs showed a higher amplitude of NMDA eEPSCs (Figure 6D) and a lower AMPA/NMDA ratio (Figure 6E). These data confirmed that NMDAR-mediated synaptic transmission was enhanced in CPNs with age.

We further assessed the susceptibility of CPNs to NMDAR-mediated epileptiform activities after postnatal week 8 by local pressure ejection of Asp, an NMDAR agonist (Errico et al., 2015), to distal apical dendrites. Application of Asp induced significantly larger inward currents in CPNs than in tdT+ neurons (*Tsc1*WT) from CTRL mice and tdT+ normal-sized *Tsc1*KO neurons (Figure 7A). In current-clamp mode, Asp evoked AP firing and membrane depolarization in *Tsc1*WT neurons and CPNs, with APs blocked by TTX and membrane depolarization by MK-801(Figures 7B and 7C). Compared with *Tsc1*WT neurons, all CPNs exhibited a significantly prolonged membrane depolarization plateau potential on which was superimposed a series of APs after the initial burst firing (Figures 7B-7D). Remarkably, MK-801 alone was sufficient to abolish the depolarization plateau potential and APs (Figures 7E and 7F), suggesting that the bursting activities of CPNs result from the prolonged membrane depolarization maintained by NMDAR activation. The same effects of TTX and MK-801 could be detected in voltage-clamp mode (Figures S7D and S7E).

The increased susceptibility of CPNs to NMDAR-mediated seizure activities was confirmed in an *in vitro* brain slice model of epilepsy, in which Mg^{2+} is omitted from artificial cerebrospinal fluid (ACSF), which releases the blockade of NMDA receptors and results in PDS-like epileptiform activities (Figure S7F). These seizure-like events can be partially blocked by the AMPAR antagonist CNQX (6-Cyano-7-nitroquinoxaline-2,3-dione) but completely suppressed by the NMDAR blocker D-AP5 (D-(−)-2-Amino-5-phosphonopentanoic acid) (Figure S7G) or MK-801 (data not shown). Compared with *Tsc1*WT neurons, CPNs generated more frequent giant inward currents with increased

amplitude and superimposed seizure-like bursts, which can also be abolished by NMDAR blockers (Figures S7H-S7J).

Cortical hyperexcitability in Tsc1CKO mice

Seizure-like burst firing recorded in CPNs at single-cell levels may suggest a larger network of synchronized neuronal activities. To test this possibility, we performed extracellular multi-electrode array recording in brain slices from CTRL and CKO mice after postnatal week 8, as in Gill et al. (2020). Raw extracellular signals were digitally filtered to extract local field potentials (LFPs) and multiunit activity (MUA), and neuronal firing was quantified across cortical depth. Cortical spiking was rare in CTRL and CKO slices when bathed in normal ACSF (data not shown). Under Mg^{2+}-free conditions, substantial neuronal spiking activities, indicated by large deflections in the MUA signal (Figure 7G), occurred in the middle to deep cortical layers but rarely in the upper cortex of CTRL slices. In contrast, CKO slices showed significantly more long-lasting bursts of spikes in the upper cortical regions that were enriched for CPNs (Figures 7G and 7H). The increase in unit spiking activities in CKO slices was coupled with increased bursting of low-amplitude, fast-frequency LFPs across cortical depth (Figure 7G), indicative of synchronized neuronal and synaptic activities. Our data suggest that the presence of CPNs promotes cortical hyperexcitability and seizure-like burst firing throughout the cortex.

DISCUSSION

In this study, we assessed the effect of late embryonic RGC *Tsc1* inactivation on TSC-related neuropathology and behavioral deficits. Targeting RGCs at the end of embryonic corticogenesis in our mice results in *Tsc1* deletion in a relatively small number of upper cortical pyramidal neurons, producing a mosaic of non-recombinant *Tsc1*WT and recombinant *Tsc1*KO upper cortical pyramidal neurons in a single animal. The prolonged lifespan allows us to interrogate underlying epileptogenic processes that lead to seizures. By characterizing *Tsc1*KO neurons and astrocytes at different ages before and after first-time seizures, we provide evidence that enhanced excitatory synaptic transmission in CPNs contributes to cortical hyperexcitability and epileptogenesis, whereas astrocyte gliosis is secondary to seizures. Our study extends the existing research in embryonic NPC models of TSC and further supports the effect of embryonic timing of *Tsc1/2* inactivation on the pathology and manifestations of TSC; loss of *Tsc1/2* at different embryonic ages may translate into complexity in terms of affected cell types, neuronal migration, and the number and anatomical or physiological changes of affected neurons, resulting in heterogeneity at cellular, circuit, and network levels, leading to phenotypic variability.

mTOR hyperactivation in early, mid-, and late gestational stages influences neuronal excitability in multiple ways, leading to divergent changes in intrinsic membrane properties (i.e., RMP), dendritic spine density, and synaptic transmission. For example, Tsc1 ablation in differentiating neurons at E13 via a synapsin (Syn1) promoter-driven Cre recombinase (Meikle et al., 2007, 2008) led to early-onset seizures starting at P5, followed by a reduction in dendritic spine density at P30. In IUE models electroporated with a constitutively active form of S16H Rheb ($Rheb^{CA}$) at E15.5, sEPSC frequency and spine density were

decreased in layer 2/3 pyramidal neurons in the prefrontal cortex (PFC) (Hsieh et al., 2020) and anterior cingulate cortex (ACC) (Lin et al., 2016). These $Rheb^{CA}$-overexpressing neurons had depolarized RMPs because of ectopic expression of the ion channel HCN4 in response to overactive mTOR (Hsieh et al., 2020). IUE of a dominant-active $Rheb^{P37L}$ mutation at E14.5 had no effect on RMPs but accelerated axonal overgrowth in $Rheb^{P37L}$-overexpressing SSC pyramidal neurons (Proietti Onori et al., 2021), whereas IUE of *Tsc1* CRISPR-Cas9 guide RNA (gRNA) at E14-E15 resulted in hyperpolarized RMPs in *Tsc1*-null neurons (Goz et al., 2020). In our mice, RMPs remained intact in CPNs, and we instead found an increase in dendritic spine density and EPSC frequencies in CPNs at postnatal week 4. The discrepancies between model systems could be attributed to differences in (1) mTOR-activating manipulations (i.e., overexpression of constitutively active Rheb versus biallelic *Tsc1* knockdown or conventional Cre-mediated *Tsc1* gene depletion), (2) embryonic timing of Tsc1 loss (E13 in Syn 1-Cre-mediated *Tsc1*CKO mice and E14-E15 in IUE mice versus E18 in our mice), (3) the duration and levels of embryonic mTOR hyperactivation, (4) brain regions (PFC and ACC versus SSC) and postnatal ages to evaluate synaptic densities and activities, and (5) the presence of early-onset seizure activities prior to the age of recording.

We noted that not all neuronal progeny from late embryonic *Tsc1*-null RGCs become cytomegalic. CPNs were instead found interspersed with normal-sized *Tsc1*KO neurons, and the numbers of CPNs varied between individual CKO mice. It is likely that the normal-sized *Tsc1*KO neurons have developed feedback mechanisms that activate compensatory responses to uncontrolled mTOR signaling (Harrington et al., 2004; Manning et al., 2005), but we consider a perinatal critical time period during which layer 2/3 neurons may require functional *Tsc1*. Some late-born *Tsc1KO* neurons can migrate into the cortical plate soon after their birth, whereas others temporarily accumulate in the subventricular zone and migrate to the cortex until the end of the first postnatal week (Polleux et al., 1997; Zgraggen et al., 2012; Rosário et al., 2012). This stochastic perinatal timing of neuronal migration, together with heterogeneous local micro-environments, may result in varying degrees of mTOR hyperactivation at different stages of neuronal development, affecting the probability and the number of individual late-born *Tsc1*KO neurons to become cytomegalic. Supporting this hypothesis, mTOR hyperactivity levels (Nguyen et al., 2019) and the timing of embryonic mTOR overactivation (Normand et al., 2013; Magri et al., 2013) have been shown to influence development of cytomegaly.

Our data demonstrate CPNs to be a major contributing factor to epileptogenesis. The presence of lower numbers of CPNs at young ages may place the brain below the seizure threshold, resulting in abnormal neural activity associated with cognitive and social deficits. With age, the growing number of CPNs, together with strengthened NMDAR-mediated synaptic transmission, predisposes the mice to spontaneous seizures. *Tsc1* deletion alters synaptic function of CPNs in a direction that favors increased glutamate-mediated excitation with an intact inhibitory synaptic input. At postnatal week 4, prior to seizures, CPNs showed increased dendritic spine density and EPSC frequency than adjacent *Tsc1*WT and normal-sized *Tsc1* KO pyramidal neurons, indicating a cell-autonomous effect of *Tsc1* deficiency. At postnatal week 8, EPSC amplitude became significantly larger, in line with an increase in NMDAR-mediated synaptic currents and upregulation of the NMDAR subunits NR2A

and NR2C in CPNs. Our data, together with recent findings showing that upregulated NR2C initiates seizures in the *Tsc1*$^{+/-}$ mice (Lozovaya et al., 2014), support an essential role of NMDAR in development of epilepsy. Prolonged depolarizing potentials can be triggered in CPNs upon NMDAR activation, resulting in long-duration, large-amplitude, paroxysmal epileptiform discharges.

Enhanced NMDAR-mediated glutamatergic synaptic transmission in CPNs, along with the synchronized spiking activities revealed by multi-electrode array (MEA) recordings, provides a cellular mechanism for cortical hyperactivity and epileptogenesis. In TSC human brains, cytomegalic dysplastic neurons are present in perituberal areas (Sosunov et al., 2015), and seizures may initiate from these non-tuberal tissues (Major et al., 2009; Ma et al., 2012). Hence, our mice, although tuber-free, represent an experimental model for the hallmark neuronal pathology of human TSC and, as a result, a valuable tool to understand the role of human dysplastic neurons in epileptogenesis.

Enhanced synaptic excitation without disinhibition has also reported in *Tsc1*-null striatonigral neurons (Benthall et al., 2018), but acute postnatal *Tsc1* loss in hippocampal CA1 neurons led to a cell-autonomous disinhibition with an intact glutamatergic synaptic drive (Bateup et al., 2013). The discrepancy between studies could be due to differences in neuronal types, the timing of *Tsc1* loss (postnatal versus embryonic *Tsc1* deletion), the duration of mTOR hyperactivation (acute versus chronic), and changes in network activities. Although affecting synaptic transmission in different ways, the net effect of *Tsc1* loss appears to be an increase in excitatory/inhibitory synaptic ratio, resulting in hyperexcitability at the network level.

Early studies also point to a causal role of *Tsc1*KO astrocytes in epileptogenesis in *hGFAP1-Cre* mediated *Tsc1*$^{hGFAP1–Cre}$ CKO mice (Uhlmann et al., 2002; Wong et al., 2003; Jansen et al., 2005). However, *hGFAP1*-Cre mediated recombination begins around E14.5 (Zeng et al., 2010), leading to *Tsc1* inactivation in astrocytes and a fraction of cortical and hippocampal CA1 neurons, which may confound interpretation of the cellular origin of seizures (Zou et al., 2017). By characterizing astrocytes in our mice at different ages and in mice with or without seizures, we showed that *Tsc1*-null astrocytes were functionally normal prior to onset of first-time seizures. The subtle increase in Gfap protein levels at postnatal week 4 may represent a cell-autonomous response to altered mTOR signaling, which was not accompanied by changes in astrocyte-regulated synaptogenesis, astrocyte glutamate uptake, and potassium buffering. By inactivating *Tsc1* more selectively in astrocytes using a tamoxifen-induced *hGFAP-Cre*ER mouse, we confirmed the lack of seizures, astrocyte gliosis, and astrocyte glutamate uptake deficits after astrocyte *Tsc1* inactivation. Our results contrast with recent observations of seizures in a different *Tsc1*$^{hGFAP\text{-}Cre\text{ER}}$CKO mouse model induced by tamoxifen (Zou et al., 2017). Again, this discrepancy may be due to use of different CreER mouse lines and, therefore, the cell type specificity of Cre recombination and the number of *Tsc1*KO neurons involved.

Our data suggest that astrocyte *Tsc1* inactivation is insufficient to trigger first-time seizures. However, we observed astrogliosis and partial loss of astrocyte glutamate transporters in CKO mice with seizures. Our results corroborate recent studies in experimental focal

cortical dysplasia mice (Feliciano et al., 2011; Hsieh et al., 2016) in which astrocyte mTOR hyperactivation and astrogliosis were induced by seizures. It remains possible that astrocyte gliosis in response to initial seizures may exacerbate synaptic hyperexcitability and contribute to disease progression of epilepsy. In line with this assumption, facilitating astrocyte glutamate uptake has been reported to suppress seizure frequency and severity in $Tsc1^{hGFAP1\text{-}Cre}CKO$ mice (Zeng et al., 2010), suggesting that enhancing astrocyte function may have therapeutic effects on epileptic seizures.

Limitations of the study

This study establishes an essential role of CPNs in cortical hyperexcitability and initial development of TSC-related epilepsy, but it remains undetermined how CPNs develop and why not all *Tsc1*KO neurons become cytomegalic. Although our analysis supports normal astrocytic regulation on synapse development and synaptic transmission prior to development of first-time seizures, it does not exclude the contribution of astrocyte gliosis to development of recurrent seizures after initial seizure events. Challenged by the multilineage potential of embryonic RGCs and the presence of *Tsc1*-null normal sized neurons and astrocytes, we were unable to specifically silence CPNs *in vivo*, and we did not perform *in vivo* rescue experiments to assess the relationship between CPNs and social/cognitive deficits. Future studies using single-cell techniques may uncover mechanisms underlying the development of CPNs and the compensatory or restorative responses to *Tsc1* inactivation in normal-sized *Tsc1*KO neurons; both will suggest novel molecular targets for specific interventions in CPNs. It is also likely that the structural abnormalities of CPNs can be prevented by mTOR inhibitors (Cox et al., 2018), but we did not test this possibility in our mice. Nevertheless, each affected neuronal process associated with cytomegaly (e.g., axonal branching, dendritic arborization, or dendritic spine morphogenesis) may require a distinct developmental critical period that is sensitive to mTOR overactivation. Future studies targeting specific pre- and perinatal critical periods should be considered.

STAR★METHODS

RESOURCE AVAILABILITY

Lead contact—Further information and requests for resources and reagents should be directed to and will be fulfilled by the Lead contact, Guomei Tang (gt2107@cumc.columbia.edu).

Material availability—All material generated in this study will be available from the lead contact with a completed Materials Transfer Agreement.

Data and code availability

- Raw and processed RNA-seq data are available on Gene Expression Omnibus (GEO) under the accession GEO:GSE156891.
- This paper does not report original code.
- Any additional information required to reanalyze the data reported in this paper is available from the Lead contact upon request.

EXPERIMENTAL MODEL AND SUBJECT DETAILS

MOUSE models— *Tsc1*$^{flox/flox}$ (#005680), *mGfap*-Cre (#012886), *hGFAP*-CreER (#012849), and Cre reporter mice (Ai9, #007909; Rosa-EYFP, #006148 and RiboTag, #029977) were obtained from Jackson Labs. We crossed *Tsc1*$^{flox/flox}$ mice with *mGfap*-Cre and Ai9 reporter mice to generate *Tsc1*$^{flox/+}$ male and *Tsc1*$^{flox/+}$*:mGfap*-Cre+:*Ai9+* female breeders. These breeding mice were of mixed genetic backgrounds (B6, 129 SvJae), and were backcrossed to the *Tsc1*$^{flox/flox}$ founder mice for 3–4 generations. *Tsc1*$^{flox/+}$*:mGfap*-Cre+;*Ai9+* female mice were then crossed to *Tsc1*$^{flox/+}$ male mice to generate *Tsc1*$^{mGfap\text{-}Cre}$CKO:*Ai9+* and *mGfap*-Cre+:*Ai9+* littermate control mice. The same breeding strategies were used to generate *Tsc1*$^{mGfap\text{-}Cre}$CKO:RiboTag and *mGfap-Cre*:RiboTag littermate control mice, and *Tsc1*$^{mGfap\text{-}Cre}$CKO:Rosa-EGFP and *mGfap-Cre*:Rosa-EGFP littermate control mice. We also crossed *Tsc1*$^{flox/flox}$ mice to *hGFAP-Cre*ER and Ai9 mice to obtain the inducible *Tsc1*$^{hGFAP\text{-}Cre\text{ER}}$CKO:*Ai9+* mice and *hGFAP-Cre*ER:*Ai9+* littermate control mice. *hGFAP-Cre*ER:*Ai9+ and Tsc1*$^{hGFAP\text{-}Cre\text{ER}}$CKO:*Ai9+* mice were treated with 10mg/ml tamoxifen (Sigma #T5648) in corn oil (Sigma C8267)) intraperitoneally at 2mg/20g body weight, one dose every other day for 5 doses starting from P14. All mouse experimental procedures were reviewed and approved by Columbia University Medical Center Institutional Animal Care and Use Committee. Mice were maintained in pathogen free conditions under a 12/12 h light/dark cycle, and housed in individually ventilated cages containing cob bedding and environmental enrichment with food and water ad libitum. For genotyping, tissues or tail tips were lysed in DNA lysis buffer (100 mM Tris-Cl, pH 8.1, 200 mM NaCl, 5 mMEDTA, 0.2% SDS) with proteinase K. Genomic DNA were extracted and subjected to PCR, using standard Jackson lab protocols for each mouse line. For all experiments, both sexes were used unless specified. Mice were subjected to histological analysis at embryonic ages of E16-E21 and postnatal ages of day 1, day 3, 4 weeks, 8 weeks and 15 weeks, to biochemical analysis and slice electrophysiology at postnatal weeks of 4, 8, and 15. We assessed autism-like behaviors and cognitive function at postnatal weeks 4–5, and seizure behaviors between postnatal weeks 4 and 28.

METHOD DETAILS

Behavioral analysis—Mice were tested at postnatal weeks 4–5 for sociability and social novelty, Novel object recognition, self-grooming repetitive behavior, contextual and feared memory, anxiety, exploratory locomotion behaviors and motor behaviors. All tests were conducted under white light between 9.00 am and 17.00 pm. All apparatuses were cleaned with 75% ethanol followed by water between sessions, trials and subjects. Spontaneous seizure behaviors were documented in home cages and confirmed by video-Electroencephalogram (EEG).

Novel object recognition was tested in a translucent arena (18.25”X13.87”X10.87”) (Tang et al., 2014). The mouse was habituated in the arena on day 1 for 10 min. On day 2, the mouse was reintroduced to the arena with two identical objects (yellow rubber ducks) placed in opposite corners, and video recorded for 15 min before returning to the home cage. After a 30-min break, the mouse was placed back into the arena, now containing one original object and one novel object (yellow cylinder) in the same opposite corners, and video recorded for

another 15-min session. Accumulative time spent sniffing the novel object vs. the original/familiar object was analyzed using Noldus Observer XT software (Noldus).

Autistic like social behaviors were assessed using the three-chamber test (Tang et al., 2014; Silverman et al., 2010) that consisted of three 10-min sessions: (1) *Habituation*: the mouse was placed in the middle chamber with the doorways into the two side chambers open, so that the mouse could explore and habituate to the empty test box; (2) *Sociability*: An unfamiliar mouse was enclosed within a wire pencil cup and placed in one side chamber. An empty wire pencil cup was placed in the other side chamber to serve as an object control. The test mouse was placed into the center chamber and allowed to explore the mouse and object in two side chambers; (3) *Preference for social novelty*: A new unfamiliar (novel) mouse was introduced into the wire pencil cup that was empty during the sociability test. The test mouse then had a choice to interact the mouse previously encountered during sociability test (familiar mouse) and the novel mouse. The apparatuses were cleaned between each session. Measures were taken of cumulative time spent sniffing the mouse and object during sociability test, and cumulative time spent sniffing the familiar or novel mouse during social novelty test. Scoring was performed by a researcher uninformed of genotype, using Noldus Observer XT software.

Spontaneous grooming behavior was assessed in a new mouse cage with a thin (1cm) layer of fresh bedding. After a 10-min habituation period, each mouse was scored with a stopwatch for 5 min for cumulative time spent grooming all body regions (Silverman et al., 2010).

Male mice were assessed for **dyadic social interactions** with unfamiliar (noncagemates) mice matched for sex and genotype. Subjects were brought into the testing room individually in clean transfer cages, and were placed in opposing corners of the test chamber (18.25”x 13.87”x 10.87”) simultaneously. Behavior was video recorded for 15 min and was coded by researchers blind to genotype using Noldus Observer XT software. Total time spent sniffing were measured.

Contextual and fear memory were tested in Plexiglas chambers (30.5X30.5X43.5 cm; Noldus). Each chamber was equipped with a stainless-steel rod floor through which the electric shock was delivered, and an upper control panel containing a video camera, a sound emitter, and a white light illuminating one corner of the chamber. During the training session, mice were exposed for 2 min to the context before applying a sound tone (30 s, 85 dB, 2800 Hz), which served as a conditioning stimulus (CS). At the end of CS, mice received a 2 s, 0.80 mA foot shock (unconditioned stimulus (US)) through the rod floor. After the CS/US pairing, mice were left in chambers for 30 s before returning to their home cage. On day 2, mice were placed back in the chamber for 5 min to assess contextual fear memory. On day 3, mice were placed in the chamber to evaluate cued fear memory. To this end, a novel context was created by decorating the chamber with black wallpaper and a smooth flat floor sprayed with vanilla odorant. After 2-min of pre-CS test, mice were exposed to the same tone used during the training session for 3 min (CS test). Freezing, characterized by lack of movement, was scored automatically using the EthoVision software (Noldus).

Anxiety and locomotion were assessed in an open field. Locomotion activities were examined by measuring total distance traveled(m). Anxiety-like behaviors were determined by measuring total time immobile(s), time in inner area(s), rearing and number of fecal boli produced. Videos were analyzed with the automated tracking program ANY-Maze (v4.82, Stoelting).

Motor coordination and balance were measured using a rotarod at an initial speed of 4 rpm, accelerating up to 40 rpm within 5 min. The time (in seconds) taken for a mouse to fall from the rod was measured. Mice were trained for 3 days, three trials per day, and tested with three trials on day 4.

Home cage behaviors were monitored in mice housed in modified home cages with clear plastic walls and water/food resources, and videotaped with a top mounted camera for 8 h/day, starting from 6 WK until behavioral seizures were documented by trained researchers according to a modified Racine scale (Cela et al., 2019), using Noldus Observer XT software (Noldus). Convulsive seizures and myoclonic seizures began at the beginning of 9WK, and seizure behaviors were mostly documented within one hour after cage change.

Video-EEG was conducted to monitor epileptic seizures. At postnatal week 7, mice were anesthetized with isoflurane and positioned on a stereotaxic frame for electrode implantation. Four small burr holes were drilled on the skull, including two bilateral holes 1 mm anterior to the bregma, one hole 2 mm posterior to the bregma on the left side, and one over the cerebellum as a reference. Four teflon-coated silver electron wires were soldered onto the pins of a microconnector (Mouser electronics, 575–501101), which was placed between the dura and the skull and covered by a non-organic dental cap. The mice were given a post-operative analgesic of carprofen (5 mg/kg, Rimadyl) subcutaneously and allowed to recover for at least 48-h prior to video-EEG monitoring. For recording, mice were connected to flexible cables to allow minimally restricted movements and recorded continuously for 48 h per week, starting from the end of postntal week 8. Signal (200 samples/s) was acquired on a Quantum 128 amplifier (Natus, Inc). Referential recordings and synchronous video were examined using Neuroworks software (Natus, Inc). Seizures or epileptiform activities were detected using Assyst (Kaoskey, Inc) and Neuroworks softwares.

RNA-seq analysis—Total RNA (RIN ≥9.8) was extracted from upper half of somatosensory/visual/retrosplenial cortices, and mRNAs were enriched using poly-A pull-down. Library was prepared using the Illumina TruSeq RNA prep kit and sequenced using an Illumina HiSeq 2000 system with a read length of 100 bases at Columbia University JP SulzBerger Genome Center. Illumina RTA software was used for base calling and bcl2fastq (version 1.8.4) software (Illumina) was used to convert BCL to fastq format, coupled with adaptor trimming, as described in Olabarria et al. (2015). The reads were mapped to a mouse reference genome (mm9) using TopHat (version 2.0.14). Differential gene expression analysis was completed using the DESeq2 pipeline, with a false discovery rate of 0.1 and an adjusted p value cut-off of 0.05 (Love et al., 2014). Gene expression heat maps were generated using Heatmap.2() function in R, using z-scaled regularized log-transformed values (scaled by row). Raw and processed RNA-seq data files were submitted to Gene Expression Omnibus (GEO).

Single nuclei extraction and PCR analysis—At the end of the recording session, cell contents were aspirated into the glass pipette by applying a gentle negative pressure (0.7–1.5 pounds per square inch). The nucleus was visibly attached to the pipette tip and extracted from the cell body. The nucleus was picked up using a second glass pipette with a larger tip of 3–4 μm in diameter, and immediately transferred into a 0.2-mL PCR tube. About 40–50 nuclei from the same type of neurons were pooled for genotyping for the conditional flox and null alleles of Tsc1, using the following primers: F4536: AGGAGGCCTCTTCTGCTACC, R4830: CAGCTCCGACCATGAAGTG, and R6548: TGGGTCCTGACC TATCTCCTA, as in Meikle et al., (2005). Amplification products are of size 486 bp for a floxed allele and 368 bp for a null allele. Upper cortical layers from somatosensory/visual/retrosplenial cortex of *Tsc1*$^{flox/flox}$ and *Tsc1*CKO mice were used as negative and positive controls for the null *Tsc1* allele.

Western blotting analysis—Mice were sacrificed by cervical dislocation. The upper half of somatosensory and parietal (visual, auditory and retrosplenial) cortices, which contains at least layers 1–3, was dissected and lysed with 1X RIPA buffer (Sigma, R0728) supplemented with protease (Roche, 11836170001) and phosphatase inhibitors (Sigma, P5726). Homogenates were centrifuged at 14,000 rpm at 4°C for 30min and supernatants were collected for total protein concentration analysis using the Bradford method (BioRad, 5000006). Protein lysates (20 μg) were mixed with NuPAGE sample buffer (Thermo Fisher Scientific, NP0007), separated in 4–12% NuPAGE Bis-Tris gels (Thermo Fisher Scientific, WG1403BOX) and transferred to Whatman PROTRAN nitrocellulose membranes (GE Healthcare, 10600001). Membranes were washed with 1X Tris-buffered saline with 0.1% Tween 20 (TBS-T, Santa Cruz Biotechnology sc-362311), and blocked with 5% dry milk in 1X TBS-T at room temperature (RT) for 1 h. The membranes were then incubated overnight with primary antibodies, washed with 1X TBS-T for 3 times at 10-min intervals, and incubated for 1h at RT with appropriate secondary antibodies. Following three 1X TBS-T washes, protein bands were visualized using Biorad Clarity™ Western ECL Substrate (Biorad, 1705061) or Clarity Max™ Western ECL Substrate (Biorad, 1705062).

Blots were imaged using the Bio-Rad ChemiDoc™ Touch Imaging System. The Signal Accumulation Mode (SAM) was used to determine the optimal exposure time for chemiluminescent detection. A series of single images with different exposure settings were then acquired. Images with saturated bands were discarded, and data analysis was performed on images where target protein bands were detected in all gel lanes. The optical densities of protein bands were quantified using Image J. Data were expressed as percentage (%) of control and presented as Mean ± SEM. 5–6 mice were used for each genotype at each age, with 3–4 technical replicates.

Immunohistochemistry (IHC) and imaging analysis—To obtain embryonic brain tissue at E16-E21, pregnant dams were deeply anesthetized with isoflurane. Embryos were removed and fixed in 4% (w/v) paraformaldehyde (PFA) for 24 h at 4°C, and cryopreserved in Tissue-Tek® O.C.T. Compound. 40 μm thick frozen coronal sections were prepared using a Leica CM3050 Cryostat and processed for IHC as free floating sections. To collect fixed brain tissue at ages of postnatal weeks 4, 8 and 15, mice were anesthetized with

isoflurane and intracardially perfused with 0.1M PBS (PH7.4) and 4% paraformaldehyde (PFA) (w/v). Brains were removed and postfixed in 4% PFA at 4°C for 24h. 40 μm thick coronal sections that contains somatosensory, auditory or visual cortices were prepared with a Leica VT1000S vibratome and stored in cryoprotectant solution at −20°C until use.

For immunofluorescence (ICC/IF), free-floating sections were incubated in blocking solution (10% goat or donkey serum in 1XPBS) for 30 min at RT, then with primary antibodies at 4°C overnight. Following 3 washes with 1XPBS/0.2% Triton-X, sections were then incubated with secondary antibodies and nuclei dye DAPI (5 μg/mL; Sigma #D9542) for 1 h at RT. After 3 washes, slices were mounted on slides in Vectashield Antifade Mounting Medium (Vector Laboratories, #H-1000-10). Experiments without primary antibodies were conducted to control for the specificity of each primary antibody. For all experiments, 4–5 mice were used for each genotype/condition at each age, and 3–5 coronal sections containing somatosensory and parietal cortices taken at different rostro-caudal levels were used from each mouse.

Z-stacks of 6 image planes (pixel size 1024 X 1024, step interval 0.5 μm, image area 606 x 606 μm were acquired using a Nikon Ti Eclipse confocal microscope, and processed with ImageJ software. To quantify the number of neurons, sections were stained for NeuN. Ten random fields were imaged from each section, and NeuN positive tdT + or tdT-cells were counted from merged images using Image J.

The relationship between levels of Gfap immunoreactivity and the number of CPNs was evaluated using image stacks acquired from *Tsc1*CKO:Ai9+ brain sections co-labeled for Gfap and NeuN. Merged images were transferred to Image J, grayscaled and analyzed for Gfap optical density (OD) and CPN numbers.

To measure Gfap, GLT1 and p-S6 levels from individual astrocytes, image stacks were acquired from *mGfap*-Cre+:Ai9+ control and *Tsc1*CKO:Ai9+ brain sections co-immunostained for S100β and GLT1, p-S6 or Gfap. A circular region-of-interest (ROI) measuring 12 μm in diameter was made for individual S100b+/tdT+ astrocytes, and Gfap, GLT1 or p-S6 fluorescence for each ROI was determined. The ROI was centered on the nucleus and included astrocyte cell body and proximal processes. Only astrocytes with clearly outlined nuclei from the merged images were included for analysis.

To determine neuronal soma size, Image stacks (295 X 295 μm) were acquired from sections co-stained for p-S6 and NeuN. Soma diameter was measured perpendicular to the basal-apical axis of neuronal soma that were outlined by tdT, p-S6, and NeuN fluorescence. Only neurons with clearly defined nuclear borders from the merged images were included for analysis.

Lucifer yellow dye fill and Sholl analysis of neuronal morphology—To determine dendritic morphology, Lucifer Yellow (Sigma #L-0259, final concentration 0.05–0.1%) was included in the patch pipette solution. Following patch clamp recording, brain slices were fixed with 4% PFA, and immunostained for Lucifer yellow. Confocal image stacks (pixel size 1024 X 1024, image size 295 X 295 μm, step size 0.3 μm) were acquired, and the

merged images were subjected to sholl analysis using Image J, with concentric rings placed centering on the cell soma. Total number of intersections between the dendrites and the shells was calculated.

DiOlistic labeling of dendritic spines and imaging—Anesthetized mice were transcardially perfused with 4% PFA. Brains were removed and immediately sectioned coronally at 200 μm using a Leica VT1000S Vibratome. Slices that contains somatosensory, auditory or visual cortices were labeled with DiO (Thermofisher Scientific, #D275) using a Helios gene gun system at 120 pounds per square inch (psi). Z stack images (pixel size 1024 X 1024, image size 42 X 42 μm, step size 0.2 μm) were acquired with a Leica multiphoton system. Segments of basal dendrites 70–100 μm distant from the soma, immediately after the first branching point, were imaged, as described in Tang et al. (2014). 15–20 DiO labeled upper cortical tdT+ or tdT− pyramidal cells were randomly chosen for analysis and 3–4 dendritic segments per neuron were analyzed. Z-stack images were reconstructed using Imaris software FilamentTracer module (Bitplane) and spine analysis was performed using ImarisXT module. Mature mushroom spines were defined as dendritic protrusions with head/neck diameter ratio 1.1 (Harris et al., 1992; Tang et al., 2014).

***In vitro* physiology—**Mice were sacrificed by cervical dislocation, and brains were removed rapidly and placed in ice-cold sucrose-based solution (in mM): 210 Sucrose, 2.5 KCl, 26 $NaHCO_3$, 1.25 NaH_2PO_4, 0.5 $CaCl_2$, 7 $MgCl_2$, 10 D-glucose. Coronal slices containing somatosensory, auditory or visual cortices were cut 180–200 μm thick for patch-clamping and 400 μm thick for multi-electrode array (MEA) recording, using a Leica VT1000S Vibratome. The slices were recovered at 34°C in artificial CSF (ACSF) (in mM): 125 NaCl, 2.5 KCl, 26 $NaHCO_3$, 1.25 NaH_2PO_4, 1.5 $CaCl_2$, 1.5 $MgCl_2$, 10 D-glucose for 18 min, and maintained in ACSF at RT for at least 42 min before recording.

Slices were then transferred to a submerged recording chamber and perfused with oxygenated ACSF (3 mL/min) at 32°C. Cells were visualized under a LEICA DM LFS microscope in the IR-DIC mode and CPNs were identified in the fluorescence mode based on their tdT fluorescence, pyramidal shape, enlarged soma size (>20 μm) and location within 350 μm from the pial surface.

Cells were patched using a glass pipette (tip resistance, 3–5 mΩ) filled with intracellular pipette solution (in mM): 130 K-gluconate, 10 KCl, 10 HEPES, 0.2 EGTA, 0.3 $CaCl_2$, 1 $MgCl_2$, 3 Mg-ATP, 0.3 Na-GTP (pH 7.3 with KOH). Action potential (AP) were elicited by somatic depolarizing current injection. The latency to the first AP was detected using steps of current injection with short duration (2 ms) under current clamp mode. AP frequency, AP threshold, AP duration at 50% of repolarization (APD50) and AP overshoot were determined using current steps (100–300 pA) with longer duration (300 ms).

We recorded spontaneous excitatory postsynaptic currents (EPSCs) by holding membrane potential at −70 mV using pCLAMP 8.2.0.235 and MultiClamp 700A commander (version 1.3.0.05). Miniature EPSCs were recorded with the same protocol in presence of 1 μM TTX (Tocris, #1069). To examine evoked EPSCs, a tungsten concentric bipolar microelectrode (World Precision Instruments, Inc., USA) was placed at cortical layer 1, 200 μm lateral

to the apical dendrite of recorded neurons. Extracellular stimulation (0.1 ms duration, 200 μA current intensity) was applied using an Isostim™ A320 Stimulus isolation unit (World Precision Instruments, Inc., USA). The peak of AMPAR-mediated EPSCs was measured by holding membrane potential at −70 mV, which was validated by using 10 μM AMPAR blocker NBQX (Tocris, #1044). The peak of NMDAR-mediated EPSCs was determined at + 40 mV, 50 ms from the stimulus artifact, and was validated by using 50 μM NMDAR antagonist D-APV (Tocris, #0106). Spontaneous inhibitory postsynaptic currents (IPSCs) were recorded at 0 mV and were blocked by bath application of 20 μM $GABA_A$ receptor blocker bicuculline (Tocris, #2503).

NMDAR mediated large inward currents were evoked by 1 mM D-aspartic acid (Sigma, #219096) in the presence of 1 μM TTX, 10 μM NBQX and 100 μM picrotoxin, which was applied though pressurized ejection (3 psi) from a glass pipette (tip opening 3 μm) using a Pressure System IIe (Toohey Company, NJ, USA). The puff pipette was placed at 50 μm lateral to and toward remote part of apical dendrite of recording neuron. Specific blockade of synaptic NMDA receptors was achieved by the application of MK-801 (10 μM).

Astrocyte potassium current was induced by pressure-ejection of 30 mM KCl, with the puff pipette placed 50 μm away from the cell body of tdT + astrocytes, in the presence of 1 μM TTX, 10 μM NBQX, 50 μM D-AP5 and 100 μM picrotoxin. Using a similar protocol, astrocyte glutamate transport current was induced by pressure-ejection of 1mM D-aspartic acid (Sigma, #219096) in the presence of 1μM TTX, 10μM NBQX, 50μM D-AP5 and 100μM picrotoxin. A universal glutamate transporter antagonist DL-*threo*-b-Benzyloxyaspartic acid (DL-TBOA, 200μM, Tocris #1223) was used to isolate glutamate transport component of the current.

Multi-electrode array (MEA) recording was conducted as described in Gill et al., 2020. Acute brain slices were placed on top of a 4X4 mm MEA system with 96 electrodes (10x10 grid, Blackrock Microsystems, Inc., USA), recorded for 10 min in ACSF containing 5 mM KCl and 2 mM $CaCl_2$, followed by 30 min in Mg^{2+} free ACSF solution at a flow rate of 6 mL/min. Signals from MEAs were digitized continuously at 30 KHz per channel (0.3 Hz-7.5 kHz bandpass) with a data acquisition system (CerePlex ™ Direct, Blackrock microsystem, USA). The raw MEA signals were bandpass filtered into two frequency bands (Dubey and Ray, 2016; Einevoll et al., 2013; Salelkar et al., 2018): multiunit activity (MUA, 250Hz high-pass Butterworth filtering, 4^{th} order) with Blackrock's Offline Spike Sorter (BOSS software, Blackrock Microsystems, Inc., USA) and local field potential (LFP, 250 Hz low-pass Bessel filtering, 8-pole) with Clampfit 10.7.0.3 (Molecular Device, USA). Multi-unit spikes were identified as signal peaks > 4 standard deviations (S.D.) of the noise mean for each channel with a −12 mV cutoff threshold. Channels that failed to detect more than one multiunit spike per minute were excluded from further analysis. Data from 3 to 5 "empty" electrodes outside the brain slice were averaged to subtract large random artifacts across all channels.

QUANTIFICATION AND STATISTICAL ANALYSIS

Statistical analyses were performed using Graphpad Prism software. The Kolmogorov-Smirnov test was applied to determine data normality. Differences between two groups

were analyzed by unpaired two-tailed t test, and multiple group comparisons were conducted by one-way or two-way ANOVA followed by Tukey's multiple comparisons test. Non-parametric data were analyzed with Mann-Whitney test. Correlations were analyzed using Spearman correlation test and nonlinear regression. All data were presented as Mean ± SEM. $p < 0.05$ was considered statistically significant.

Supplementary Material

Refer to Web version on PubMed Central for supplementary material.

ACKNOWLEDGMENTS

This work was supported by the Defense Health Programs and Congressionally Directed Medical Research Programs through the TSCRP under Awards W81XWH-16-1-0263 (G.T.), W81XWH-15-1-0112 (J.E.G. and G.T.) and W81XWH-12-1-0196 (D.S., J.E.G. and G.T.). Opinions, interpretations, conclusions and recommendations are those of the author and are not necessarily endorsed by the Department of Defense. Additional support was provided by the NIH/NIMH (K01 MH096956 to G.T.), NIH/NINDS (R01 NS104390 to G.T.), Simons Foundation (SFARI 402220 to G.T.), NIH/NINDS (R01 NS095435 to D.S.), NIH/NIDA (R01 DA007418 to D.S.), Simons Foundation (SFARI 514813 to D.S.), NIH/NIA (R01 AG049402 to O.A.), NIH/NINDS (R01 NS092405 to O.A.), NIH/NINDS (R01 NS110024 to O.A.), NIH/NINDS (R01 NS084142 to C.A.S.), and NIH/NINDS (R01 NS031348 to W.N.F.).

REFERENCES

Anderl S, Freeland M, Kwiatkowski DJ, and Goto J (2011). Therapeutic value of prenatal rapamycin treatment in a mouse brain model of tuberous sclerosis complex. Hum. Mol. Genet 20, 4597–4604. 10.1093/hmg/ddr393. [PubMed: 21890496]

Atasoy D, Ertunc M, Moulder KL, Blackwell J, Chung C, Su J, and Kavalali ET (2008). Spontaneous and evoked glutamate release activates two populations of NMDA receptors with limited overlap. J. Neurosci 28, 10151–10166. 10.1523/JNEUROSCI.2432-08.2008. [PubMed: 18829973]

Bateup HS, Johnson CA, Denefrio CL, Saulnier JL, Kornacker K, and Sabatini BL (2013). Excitatory/inhibitory synaptic imbalance leads to hippocampal hyperexcitability in mouse models of tuberous sclerosis. Neuron 78, 510–522. 10.1016/j.neuron.2013.03.017. [PubMed: 23664616]

Benthall KN, Ong SL, and Bateup HS (2018). Corticostriatal transmission is selectively enhanced in striatonigral neurons with postnatal loss of Tsc1.Cell Rep. 23, 3197–3208. 10.1016/j.celrep.2018.05.037. [PubMed: 29898392]

Bolton PF, and Griffiths PD (1997). Association of tuberous sclerosis of temporal lobes with autism and atypical autism. Lancet 349, 392–395. 10.1016/S0140-6736(97)80012-8. [PubMed: 9033466]

Bolton PF, Clifford M, Tye C, Maclean C, Humphrey A, le Maréchal K, Higgins JNP, Neville BG, Rijsdjik F, and Tuberous Sclerosis 2000 Study Group; and Yates JRW (2015). Intellectual abilities in tuberous sclerosis complex: risk factors and correlates from the tuberous sclerosis 2000 study. Psychol. Med 45, 2321–2331. 10.1017/S0033291715000264. [PubMed: 25827976]

Buckmaster PS, and Lew FH (2011). Rapamycin suppresses mossy fiber sprouting but not seizure frequency in a mouse model of temporal lobe epilepsy. J. Neurosci 31, 2337–2347. 10.1523/JNEUROSCI.4852-10.2011. [PubMed: 21307269]

Carson RP, Van Nielen DL, Winzenburger PA, and Ess KC (2012). Neuronal and glia abnormalities in Tsc1-deficient forebrain and partial rescue by rapamycin. Neurobiol. Dis 45, 369–380. 10.1016/j.nbd.2011.08.024. [PubMed: 21907282]

Cela E, McFarlan AR, Chung AJ, Wang T, Chierzi S, Murai KK, and Sjöström PJ (2019). An optogenetic kindling model of neocortical epilepsy. Sci. Rep 9, 5236. 10.1038/s41598-019-41533-2. [PubMed: 30918286]

Cepeda C, André VM, Yamazaki I, Hauptman JS, Chen JY, Vinters HV, Mathern GW, and Levine MS (2010). Comparative study of cellular and synaptic abnormalities in brain tissue samples

from pediatric tuberous sclerosis complex and cortical dysplasia type II. Epilepsia 51, 160–165. 10.1111/j.1528-1167.2010.02633.x. [PubMed: 20618424]

Chung WS, Allen NJ, and Eroglu C (2015). Astrocytes control synapse formation, function, and elimination. Cold Spring Harb. Perspect. Biol 7, a020370. 10.1101/cshperspect.a020370. [PubMed: 25663667]

Cox RL, Calderon de Anda F, Mangoubi T, and Yoshii A (2018). Multiple critical periods for rapamycin treatment to correct structural defects in Tsc-1-suppressed brain. Front. Mol. Neurosci 11, 409. 10.3389/fnmol.2018.00409. [PubMed: 30467464]

Crino PB (2013). Evolving neurobiology of tuberous sclerosis complex. Acta Neuropathol. 125, 317–332. 10.1007/s00401-013-1085-x [PubMed: 23386324]

Curatolo P, and Maria BL (2013). Tuberous sclerosis. Handb. Clin. Neurol 111, 323–331. 10.1016/B978-0-444-52891-9.00038-5. [PubMed: 23622183]

Desai AR, and McConnell SK (2000). Progressive restriction in fate potential by neural progenitors during cerebral cortical development. Development 127, 2863–2872. 10.1242/dev.127.13.2863. [PubMed: 10851131]

Dubey A, and Ray S (2016). Spatial spread of local field potential is bandpass in the primary visual cortex. J. Neurophysiol 116, 1986–1999. 10.1242/dev.127.13.2863. [PubMed: 27489369]

Einevoll GT, Kayser C, Logothetis NK, and Panzeri S (2013). Modelling and analysis of local field potentials for studying the function of cortical circuits. Nat. Rev. Neurosci 14, 770–785. 10.1038/nrn3599. [PubMed: 24135696]

Errico F, Mothet JP, and Usiello A (2015). D-Aspartate: an endogenous NMDA receptor agonist enriched in the developing brain with potential involvement in schizophrenia. J. Pharm. Biomed. Anal 116, 7–17. 10.1016/j.jpba.2015.03.024. [PubMed: 25868730]

Feliciano DM, Su T, Lopez J, Platel JC, and Bordey A (2011). Single-cell Tsc1 knockout during corticogenesis generates tuber-like lesions and reduces seizure threshold in mice. J. Clin. Invest 121, 1596–1607. 10.1172/JCI44909. [PubMed: 21403402]

Ganat YM, Silbereis J, Cave C, Ngu H, Anderson GM, Ohkubo Y, Ment LR, and Vaccarino FM (2006). Early postnatal astroglial cells produce multilineage precursors and neural stem cells in vivo. J. Neurosci 26, 8609–8621. 10.1523/JNEUROSCI.2532-06.2006. [PubMed: 16914687]

Garcia ADR, Doan NB, Imura T, Bush TG, and Sofroniew MV (2004). GFAP-expressing progenitors are the principal source of constitutive neurogenesis in adult mouse forebrain. Nat. Neurosci 7, 1233–1241. 10.1038/nn1340. [PubMed: 15494728]

Gill BJA, Wu X, Khan FA, Sosunov AA, Liou JY, Dovas A, Eissa TL, Banu MA, Bateman LM, McKhann GM 2nd., et al. (2020). Ex vivo multi-electrode analysis reveals spatiotemporal dynamics of ictal behavior at the infiltrated margin of glioma. Neurobiol. Dis 134, 104676. 10.1016/j.nbd.2019.104676. [PubMed: 31731042]

Glowatzki E, Cheng N, Hiel H, Yi E, Tanaka K, Ellis-Davies GC, Rothstein JD, and Bergles DE (2006). The glutamate-aspartate transporter GLAST mediates glutamate uptake at inner hair cell afferent synapses in the mammalian cochlea. J. Neurosci 26, 7659–7664. 10.1523/JNEUROSCI.1545-06.2006. [PubMed: 16855093]

Goodman M, Lamm SH, Engel A, Shepherd CW, Houser OW, and Gomez MR (1997). Cortical tuber count: a biomarker indicating neurologic severity of tuberous sclerosis complex. J. Child Neurol 12, 85–90. 10.1177/088307389701200203. [PubMed: 9075016]

Goto J, Talos DM, Klein P, Qin W, Chekaluk YI, Anderl S, Malinowska IA, Di Nardo A, Bronson RT, Chan JA, et al. (2011). Regulable neural progenitor-specific Tsc1 loss yields giant cells with organellar dysfunction in a model of tuberous sclerosis complex. Proc. Natl. Acad. Sci. USA 108, E1070–E1079. 10.1073/pnas.1106454108. [PubMed: 22025691]

Goz RU, Akgül G, and LoTurco JJ (2020). BRAFV600E expression in neural progenitors results in a hyperexcitable phenotype in neocortical pyramidal neurons. J. Neurophysiol 123, 2449–2464. 10.1152/jn.00523.2019. [PubMed: 32401131]

Harrington LS, Findlay GM, Gray A, Tolkacheva T, Wigfield S, Rebholz H, Barnett J, Leslie NR, Cheng S, Shepherd PR, et al. (2004). The TSC1-2 tumor suppressor controls insulin-PI3K signaling via regulation of IRS proteins. J. Cell Biol 166, 213–223. 10.1083/jcb.200403069. [PubMed: 15249583]

Harris KM, Jensen FE, and Tsao B (1992). Three-dimensional structure of dendritic spines and synapses in rat hippocampus (CA1) at postnatal day 15 and adult ages: implications for the maturation of synaptic physiology and long-term potentiation [published erratum appears in J Neurosci 1992 Aug;12(8):following table of contents]. J. Neurosci 12, 2685–2705. 10.1523/JNEUROSCI.12-07-02685.1992. [PubMed: 1613552]

Hotka M, and Kubista H (2019). The paroxysmal depolarization shift in epilepsy research. Int. J. Biochem. Cell Biol 107, 77–81. 10.1016/j.biocel.2018.12.006. [PubMed: 30557621]

Hsieh LS, Wen JH, Claycomb K, Huang Y, Harrsch FA, Naegele JR, Hyder F, Buchanan GF, and Bordey A (2016). Convulsive seizures from experimental focal cortical dysplasia occur independently of cell misplacement. Nat. Commun 7, 11753. 10.1038/ncomms11753. [PubMed: 27249187]

Hsieh LS, Wen JH, Nguyen LH, Zhang L, Getz SA,Torres-Reveron J, Wang Y, Spencer DD, and Bordey A (2020). Ectopic HCN4 expression drives mTOR-dependent epilepsy in mice. Sci. Transl. Med 12, eabc1492. 10.1126/scitranslmed.abc1492. [PubMed: 33208499]

Huettner JE, and Bean BP (1988). Block of N-methyl-D-aspartate-activated current by the anticonvulsant MK-801: selective binding to open channels. Proc. Natl. Acad. Sci. USA 85, 1307–1311. 10.1073/pnas.85.4.1307. [PubMed: 2448800]

Jansen LA, Uhlmann EJ, Crino PB, Gutmann DH, and Wong M (2005). Epileptogenesis and reduced inward rectifier potassium current in tuberous sclerosis complex-1-deficient astrocytes. Epilepsia 46, 1871–1880. 10.1111/j.1528-1167.2005.00289.x. [PubMed: 16393152]

Kwiatkowski DJ, Zhang H, Bandura JL, Heiberger KM, Glogauer M, el-Hashemite N, and Onda H (2002). A mouse model of TSC1 reveals sex-dependent lethality from liver hemangiomas, and up-regulation of p70S6 kinase activity in Tsc1 null cells. Hum. Mol. Genet 11, 525–534. 10.1093/hmg/11.5.525. [PubMed: 11875047]

Lee DF, Kuo HP, Chen CT, Hsu JM, Chou CK, Wei Y, Sun HL, Li LY, Ping B, Huang WC, et al. (2007). IKK beta suppression of TSC1 links inflammation and tumor angiogenesis via the mTOR pathway. Cell 130, 440–455. 10.1016/j.cell.2007.05.058. [PubMed: 17693255]

Lim JS, Gopalappa R, Kim SH, Ramakrishna S, Lee M, Kim WI, Kim J, Park SM, Lee J, Oh JH, et al. (2017). Somatic mutations in TSC1 and TSC2 cause focal cortical dysplasia. Am. J. Hum. Genet 100, 454–472. 10.1016/j.ajhg.2017.01.030. [PubMed: 28215400]

Lin TV, Hsieh L, Kimura T, Malone TJ, and Bordey A (2016). Normalizing translation through 4E-BP prevents mTOR-driven cortical mislamination and ameliorates aberrant neuron integration. Proc. Natl. Acad. Sci. USA 113, 11330–11335. 10.1073/pnas.1605740113. [PubMed: 27647922]

Liu Y, Wong TP, Aarts M, Rooyakkers A, Liu L, Lai TW, Wu DC, Lu J,Tymianski M, Craig AM, and Wang YT (2007). NMDA receptor subunits have differential roles in mediating excitotoxic neuronal death both in vitro and in vivo. J. Neurosci 27, 2846–2857. 10.1523/JNEUROSCI.0116-07.2007. [PubMed: 17360906]

Lozovaya N, Gataullina S, Tsintsadze T, Tsintsadze V, Pallesi-Pocachard E, Minlebaev M, Goriounova NA, Buhler E, Watrin F, Shityakov S, et al. (2014). Selective suppression of excessive GluN2C expression rescues early epilepsy in a tuberous sclerosis murine model. Nat. Commun 5, 4563. 10.1038/ncomms5563. [PubMed: 25081057]

Love MI, Huber W, and Anders S (2014). Moderated estimation of fold change and dispersion for RNA-seq data with DESeq2. Genome Biol. 15, 550. 10.1186/s13059-014-0550-8. [PubMed: 25516281]

Ma TS, Elliott RE, Ruppe V, Devinsky O, Kuzniecky R,Weiner HL, and Carlson C (2012). Electrocorticographic evidence of perituberal cortex epileptogenicity in tuberous sclerosis complex. J. Neurosurg. Pediatr 10, 376–382. 10.3171/2012.8.PEDS1285. [PubMed: 22998031]

Madisen L, Zwingman TA, Sunkin SM, Oh SW, Zariwala HA, Gu H, Ng LL, Palmiter RD, Hawrylycz MJ, Jones AR, Lein ES, and Zeng H (2010). A robust and high-throughput Cre reporting and characterization system for the whole mouse brain. Nat. Neurosci 13, 133–140. 10.1038/nn.2467. [PubMed: 20023653]

Magri L, Cambiaghi M, Cominelli M, Alfaro-Cervello C, Cursi M, Pala M, Bulfone A, Garcìa-Verdugo J, Leocani L, and Minicucci F (2011). Sustained activation of mTOR pathway in embryonic neural stem cells leads to development of tuberous sclerosis complex-associated lesions. Cell Stem Cell 9, 447–462. 10.1016/j.stem.2011.09.008. [PubMed: 22056141]

Magri L, Cominelli M, Cambiaghi M, Cursi M, Leocani L, Minicucci F, Poliani PL, and Galli R (2013). Timing of mTOR activation affects tuberous sclerosis complex neuropathology in mouse models. Dis. Model. Mech 6, 1185–1197. 10.1242/dmm.012096. [PubMed: 23744272]

Major P, Rakowski S, Simon MV, Cheng ML, Eskandar E, Baron J, Leeman BA, Frosch MP, and Thiele EA (2009). Are cortical tubers epileptogenic? Evidence from electrocorticography. Epilepsia 50, 147–154. 10.1111/j.1528-1167.2008.01814.x. [PubMed: 19125835]

Manning BD, Logsdon MN, Lipovsky AI, Abbott D, Kwiatkowski DJ, and Cantley LC (2005). Feedback inhibition of Akt signaling limits the growth of tumors lacking Tsc2. Genes Dev. 19, 1773–1778. 10.1101/gad.1314605. [PubMed: 16027169]

Meikle L, McMullen JR, Sherwood MC, Lader AS, Walker V, Chan JA, and Kwiatkowski DJ (2005). A mouse model of cardiac rhabdomyoma generated by loss of Tsc1 in ventricular myocytes. Hum. Mol. Genet 14, 429–435. 10.1093/hmg/ddi039. [PubMed: 15601645]

Meikle L, Talos DM, Onda H, Pollizzi K, Rotenberg A, Sahin M, Jensen FE, and Kwiatkowski DJ (2007). A mouse model of tuberous sclerosis: neuronal loss of Tsc1 causes dysplastic and ectopic neurons, reduced myelination, seizure activity, and limited survival. J. Neurosci 27, 5546–5558. 10.1523/JNEUROSCI.5540-06.2007. [PubMed: 17522300]

Meikle L, Pollizzi K, Egnor A, Kramvis I, Lane H, Sahin M, and Kwiatkowski DJ (2008). Response of a neuronal model of tuberous sclerosis to mammalian target of rapamycin (mTOR) inhibitors: effects on mTORC1 and Akt signaling lead to improved survival and function. J. Neurosci 28, 5422–5432. 10.1523/JNEUROSCI.0955-08.2008. [PubMed: 18495876]

Mietzsch U, McKenna J 3rd, Reith RM, Way SW, and Gambello MJ (2013). Comparative analysis of Tsc1 and Tsc2 single and double radial glial cell mutants. J. Comp. Neurol 521, 3817–3831. 10.1002/cne.23380. [PubMed: 23749404]

Nguyen LH, Mahadeo T, and Bordey A (2019). mTOR hyperactivity levels influence the severity of epilepsy and associated neuropathology in an experimental model of tuberous sclerosis complex and focal cortical dysplasia. J. Neurosci 39, 2762–2773. 10.1523/JNEUROSCI.2260-18.2019. [PubMed: 30700531]

Normand EA, Crandall SR, Thorn CA, Murphy EM, Voelcker B, Browning C, Machan JT, Moore CI, Connors BW, and Zervas M (2013). Temporal and mosaic Tsc1 deletion in the developing thalamus disrupts thalamocortical circuitry, neural function, and behavior. Neuron 78, 895–909. 10.1016/j.neuron.2013.03.030. [PubMed: 23664552]

Olabarria M, Putilina M, Riemer EC, and Goldman JE (2015). Astrocyte pathology in Alexander disease causes a marked inflammatory environment. Acta Neuropathol. 130, 469–486. 10.1007/s00401-015-1469-1. [PubMed: 26296699]

Polleux F, Dehay C, and Kennedy H (1997). The timetable of laminar neurogenesis contributes to the specification of cortical areas in mouse isocortex. J. Comp. Neurol 385, 95–116. 10.1002/(sici)1096-9861(19970818)385:1<95::aid-cne6>3.0.co;2-7. [PubMed: 9268119]

Proietti Onori M, Koene LMC, Schäfer CB, Nellist M, de Brito van Velze M, Gao Z, Elgersma Y, and van Woerden GM (2021). RHEB/mTOR hyperactivity causes cortical malformations and epileptic seizures through increased axonal connectivity. PLoS Biol. 19, e3001279. 10.1371/journal.pbio.3001279. [PubMed: 34038402]

Pun RY, Rolle IJ, Lasarge CL, Hosford BE, Rosen JM, Uhl JD, Schmeltzer SN, Faulkner C, Bronson SL, Murphy BL, et al. (2012). Excessive activation of mTOR in postnatally generated granule cells is sufficient to cause epilepsy. Neuron 75, 1022–1034. 10.1016/j.neuron.2012.08.002. [PubMed: 22998871]

Rimmele TS, Rocher AB, Wellbourne-Wood J, and Chatton JY (2017). Control of glutamate transport by extracellular potassium: basis for a negative feedback on synaptic transmission. Cerebr. Cortex 27, 3272–3283. 10.1093/cercor/bhx078.

Rosário M, Schuster S, Jüttner R, Parthasarathy S, Tarabykin V, and Birchmeier W (2012). Neocortical dendritic complexity is controlled during development by NOMA-GAP-dependent inhibition of Cdc42 and activation of cofilin. Genes Dev. 26, 1743–1757. 10.1101/gad.191593.112. [PubMed: 22810622]

Sahin M, Henske EP, Manning BD, Ess KC, Bissler JJ, Klann E, Kwiatkowski DJ, Roberds SL, Silva AJ, Hillaire-Clarke CS, et al. (2016). Advances and future directions for tuberous sclerosis

complex research: recommendations from the 2015 strategic planning conference. Pediatr. Neurol 60, 1–12. 10.1016/j.pediatrneurol.2016.03.015. [PubMed: 27267556]

Salelkar S, Somasekhar GM, and Ray S (2018). Distinct frequency bands in the local field potential are differently tuned to stimulus drift rate. J. Neurophysiol 120, 681–692. 10.1152/jn.00807.2017. [PubMed: 29694281]

Sanz E, Yang L, Su T, Morris DR, McKnight GS, and Amieux PS (2009). Cell-type-specific isolation of ribosome-associated mRNA from complex tissues. Proc. Natl. Acad. Sci. USA 106, 13939–13944. 10.1073/pnas.0907143106. [PubMed: 19666516]

Silverman JL, Yang M, Lord C, and Crawley JN (2010). Behavioural phenotyping assays for mouse models of autism. Nat. Rev. Neurosci 11, 490–502. 10.1038/nrn2851. [PubMed: 20559336]

Sosunov AA, Guilfoyle E, Wu X, McKhann GM 2nd, and Goldman JE (2013). Phenotypic conversions of “protoplasmic” to “reactive” astrocytes in Alexander disease. J. Neurosci 33, 7439–7450. 10.1523/JNEUROSCI.4506-12.2013. [PubMed: 23616550]

Sosunov AA, McGovern RA, Mikell CB, Wu X, Coughlin DG, Crino PB, Weiner HL, Ghatan S, Goldman JE, and McKhann GM 2nd. (2015). Epileptogenic but MRI-normal perituberal tissue in tuberous sclerosis complex contains tuber-specific abnormalities. Acta. Neuropathol. Commun 3, 17. 10.1186/s40478-015-0191-5. [PubMed: 25853525]

Srinivas S, Watanabe T, Lin CS, William CM, Tanabe Y, Jessell TM, and Costantini F (2001). Cre reporter strains produced by targeted insertion of EYFP and ECFP into the ROSA26 locus. BMC Dev. Biol 1, 4. 10.1186/1471-213x-1-4. [PubMed: 11299042]

Stafstrom CE (2010). Pathophysiological mechanisms of seizures and epilepsy: a primer. In Epilepsy: Mechanisms, Models, and Translational Perspectives (CRC Press), pp. 3–19. 10.1201/9781420085594.

Sun W, Hansen KB, and Jahr CE (2017). Allosteric interactions between NMDA receptor subunits shape the developmental shift in channel properties. Neuron 94, 58–64.e3. 10.1016/j.neuron.2017.03.018. [PubMed: 28384476]

Sutula T, Cascino G, Cavazos J, Parada I, and Ramirez L (1989). Mossy fiber synaptic reorganization in the epileptic human temporal lobe. Ann. Neurol. 26, 321–330. 10.1002/ana.410260303. [PubMed: 2508534]

Tang G, Gudsnuk K, Kuo SH, Cotrina ML, Rosoklija G, Sosunov A, Sonders MS, Kanter E, Castagna C, Yamamoto A, et al. (2014). Loss of mTOR-dependent macroautophagy causes autistic-like synaptic pruning deficits. Neuron 83, 1131–1143. 10.1016/j.neuron.2014.07.040. [PubMed: 25155956]

Tovar KR, and Westbrook GL (2002). Mobile NMDA receptors at hippocampal synapses. Neuron 34, 255–264. 10.1016/S0896-6273(02)00658-X. [PubMed: 11970867]

Uhlmann EJ, Wong M, Baldwin RL, Bajenaru ML, Onda H, Kwiatkowski DJ, Yamada K, and Gutmann DH (2002). Astrocyte-specific TSC1 conditional knockout mice exhibit abnormal neuronal organization and seizures. Ann. Neurol 52, 285–296. 10.1002/ana.10283. [PubMed: 12205640]

Way SW, McKenna J 3rd, Mietzsch U, Reith RM, Wu HCJ, and Gambello MJ (2009). Loss of Tsc2 in radial glia models the brain pathology of tuberous sclerosis complex in the mouse. Hum. Mol. Genet 18, 1252–1265. 10.1093/hmg/ddp025. [PubMed: 19150975]

Wong M, Ess KC, Uhlmann EJ, Jansen LA, Li W, Crino PB, Mennerick S, Yamada KA, and Gutmann DH (2003). Impaired glial glutamate transport in a mouse tuberous sclerosis epilepsy model. Ann. Neurol 54, 251–256. 10.1002/ana.10648. [PubMed: 12891680]

Wong M (2019). The role of glia in epilepsy, intellectual disability, and other neurodevelopmental disorders in tuberous sclerosis complex. J. Neurodev. Disord 11, 30. 10.1186/s11689-019-9289-6. [PubMed: 31838997]

Zeng LH, Bero AW, Zhang B, Holtzman DM, and Wong M (2010). Modulation of astrocyte glutamate transporters decreases seizures in a mouse model of Tuberous Sclerosis Complex. Neurobiol. Dis 37, 764–771. 10.1016/j.nbd.2009.12.020. [PubMed: 20045054]

Zgraggen E, Boitard M, Roman I, Kanemitsu M, Potter G, Salmon P, Vutskits L, Dayer AG, and Kiss JZ (2012). Early postnatal migration and development of layer II pyramidal neurons in the rodent cingulate/retrosplenial cortex. Cerebr. Cortex 22, 144–157. 10.1093/cercor/bhr097.

Zou J, Zhang B, Gutmann DH, and Wong M (2017). Postnatal reduction of tuberous sclerosis complex 1 expression in astrocytes and neurons causes seizures in an age-dependent manner. Epilepsia 58, 2053–2063. 10.1111/epi.13923. [PubMed: 29023667]

Highlights

- Tsc1-null late embryonic RGCs generate cytomegalic pyramidal neurons (CPNs)
- CPNs are synaptically hyperexcitable and susceptible to seizure-like activities
- Enhanced synaptic excitation in CPNs contributes to epileptogenesis
- Astrocyte gliosis evolves secondary to recurrent seizures

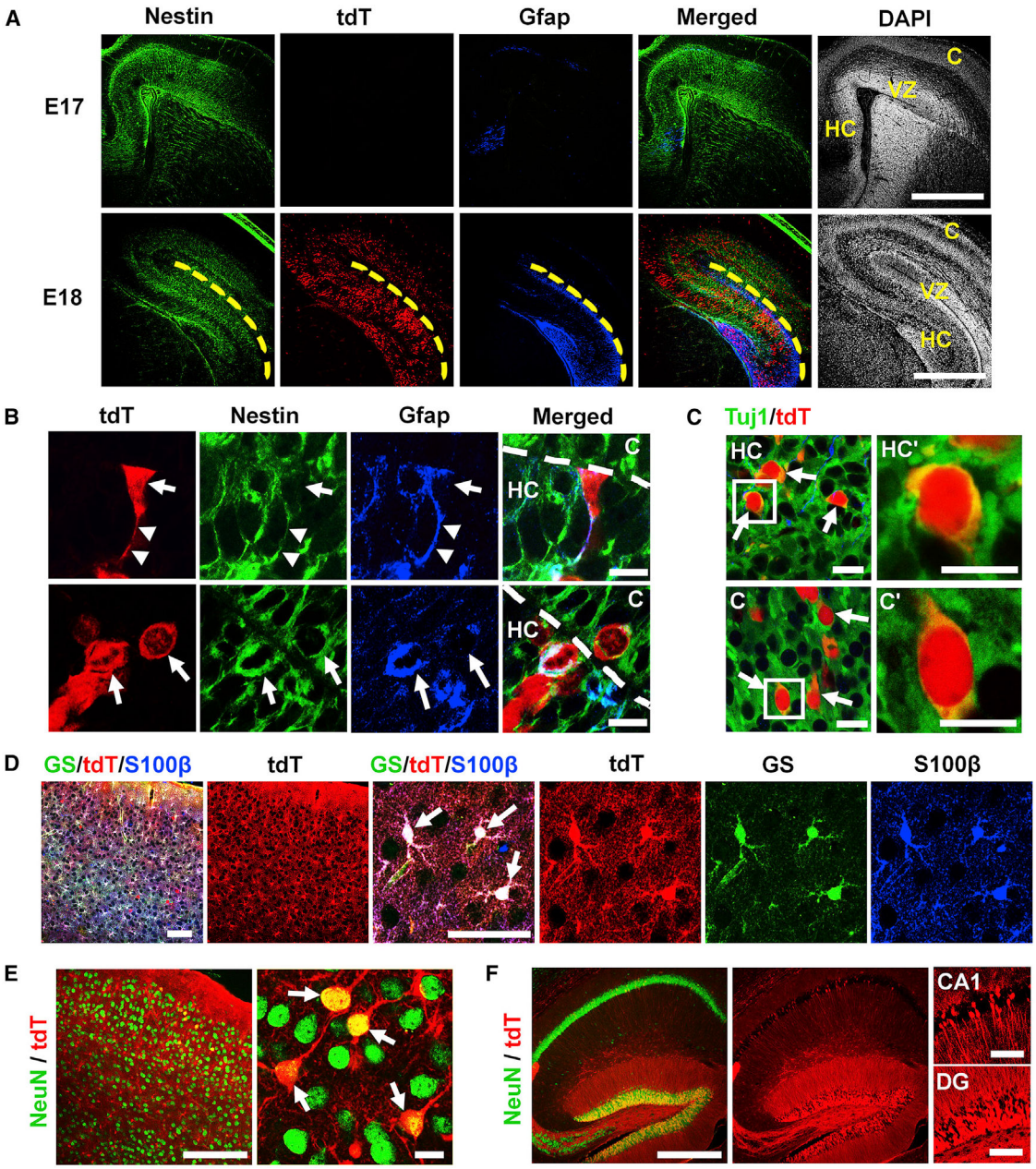

Figure 1. *mGfap*-Cre-mediated recombination in late embryonic radial glia cells (RGCs)

(A) Immunofluorescence of tdT (red), nestin (green), and Gfap (blue) in *mGfap-Cre:Ai9+* embryos at E17 and E18.

Cre-mediated recombination is indicated by tdT expression. The dotted lines show the ventricle surface. C, cortex; HC, hippocampus; VZ, ventricular zone. Scale bars, 450 μm.

(B) tdT+ RGCs (arrows) at E18, indicated by their cell bodies anchored to the ventricular surface (dotted line), radial basal processes (arrowheads), and immunoreactivities for Gfap and nestin. Scale bars, 15 μm.

(C) The presence of Tuj1+ tdT+ neurons (arrows) at E18. Scale bars, 15 μm.

(D) GS+ S100β+ tdT+ astrocytes (arrows) in the cortex of *mGfap-Cre:Ai9+* mice at postnatal week 4. Scale bars, 100 μm.
(E) NeuN+ tdT+ pyramidal neurons (arrows) in the upper cortex of *mGfap-Cre:Ai9+* mice at postnatal week 4. Scale bars, 200 μm (left) and 15 μm (right).
(F) tdT+ neurons in the hippocampus of *mGfap-Cre:Ai9+* mice at postnatal week 4. Scale bars, 200 μm (left) and 50 μm (right). At each age, 4–5 mice are used.

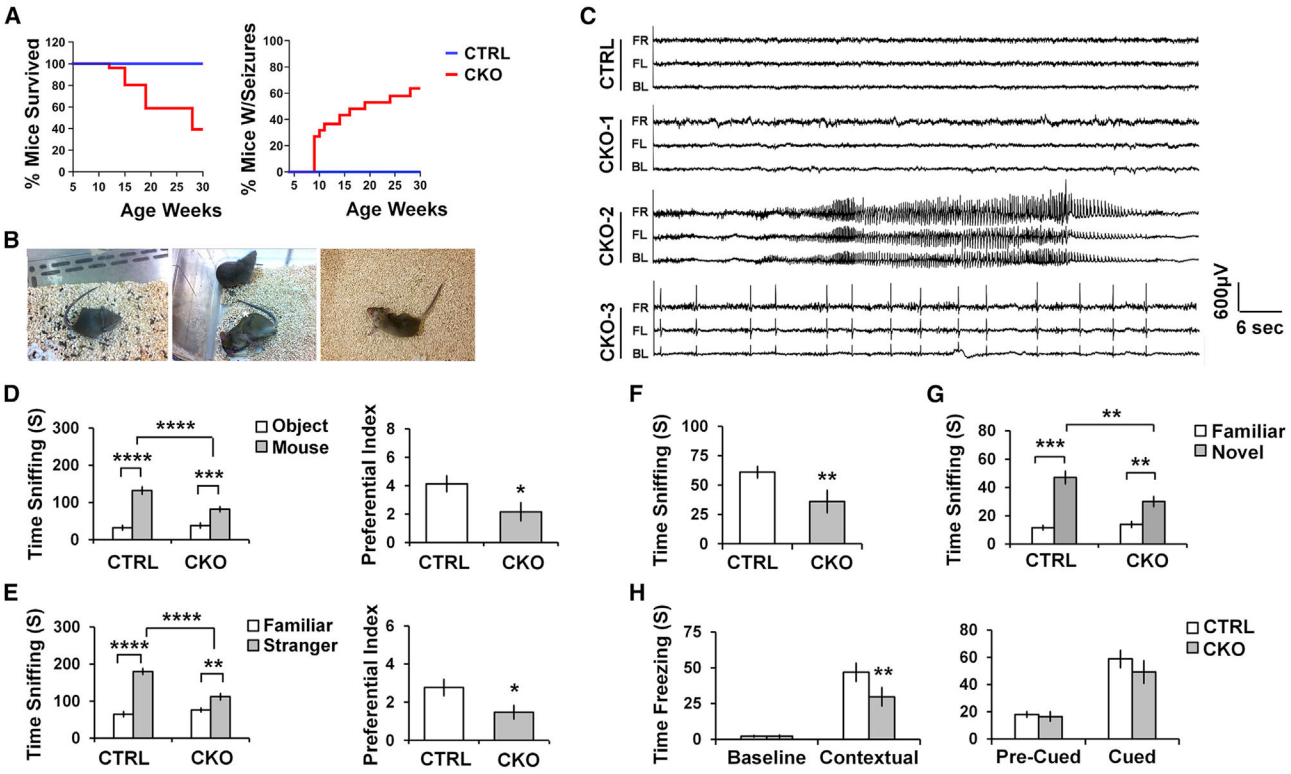

Figure 2. Neurological symptoms in *Tsc1CKO* mice

(A) Kaplan-Meier plots of survival rate (left) and accumulative incidence of behavioral seizures (right) in *mGfap*-Cre:Ai9+ control (CTRL, n = 29) and *Tsc1CKO:Ai9+* (CKO, n = 65) littermates.

(B) Single-image frames showing spontaneous seizures in CKO mice. Left: a mouse with tail rigidity and lifted forelimb. Center: a mouse (*) on its side with forelimb extension and loss of posture (Video S1). Right: a mouse losing posture and falling on one side (Video S2).

(C) Representative EEG traces recorded from epidural electrodes placed over the right frontal (RF), left frontal (LF), and back left (BL) surface of the neocortex. CKO-1, a CKO mouse with a normal EEG pattern similar to that of the CTRL; CKO-2, a CKO mouse with generalized tonic-clonic seizures (GTCSs); CKO-3, a CKO mouse showing generalized interictal epileptiform discharges. CTRL, n = 10; CKO, n = 15.

(D) 3-chamber sociability test at postnatal weeks 4–5. CTRL and CKO mice spend more time on a social versus a non-social target, but CKO mice spend less time with the mouse (left), with a reduced preference for the social target (right).

(E) 3-chamber social novelty test at postnatal weeks 4–5. CTRL and CKO mice spend more time sniffing novel versus familiar mice, but CKO mice show less interests in novel mice (left) and a reduced preference for the novel target (right).

(F) Reciprocal dyadic social interaction test at postnatal weeks 4–5. Compared with the CTRL, CKO mice spend less time interacting with a novel stimulus mouse.

(G) Novel object recognition test at postnatal weeks 4–5. CTRL and CKO mice explore a novel object, but CKO mice spend less time with the novel object.

(H) Fear conditioning test at postnatal weeks 4–5. CKO mice show impaired contextual memory (left) but intact feared memory (right).

All data are presented as mean ± SEM. **p < 0.01, ***p < 0.001, ****p < 0.0001; two-way ANOVA in (D), left; (E), left; (G); and (H). *p < 0.05, unpaired t test in (D), right; (E), right; and (F). In (D)–(H), CTRL n = 19 and CKO n = 24.

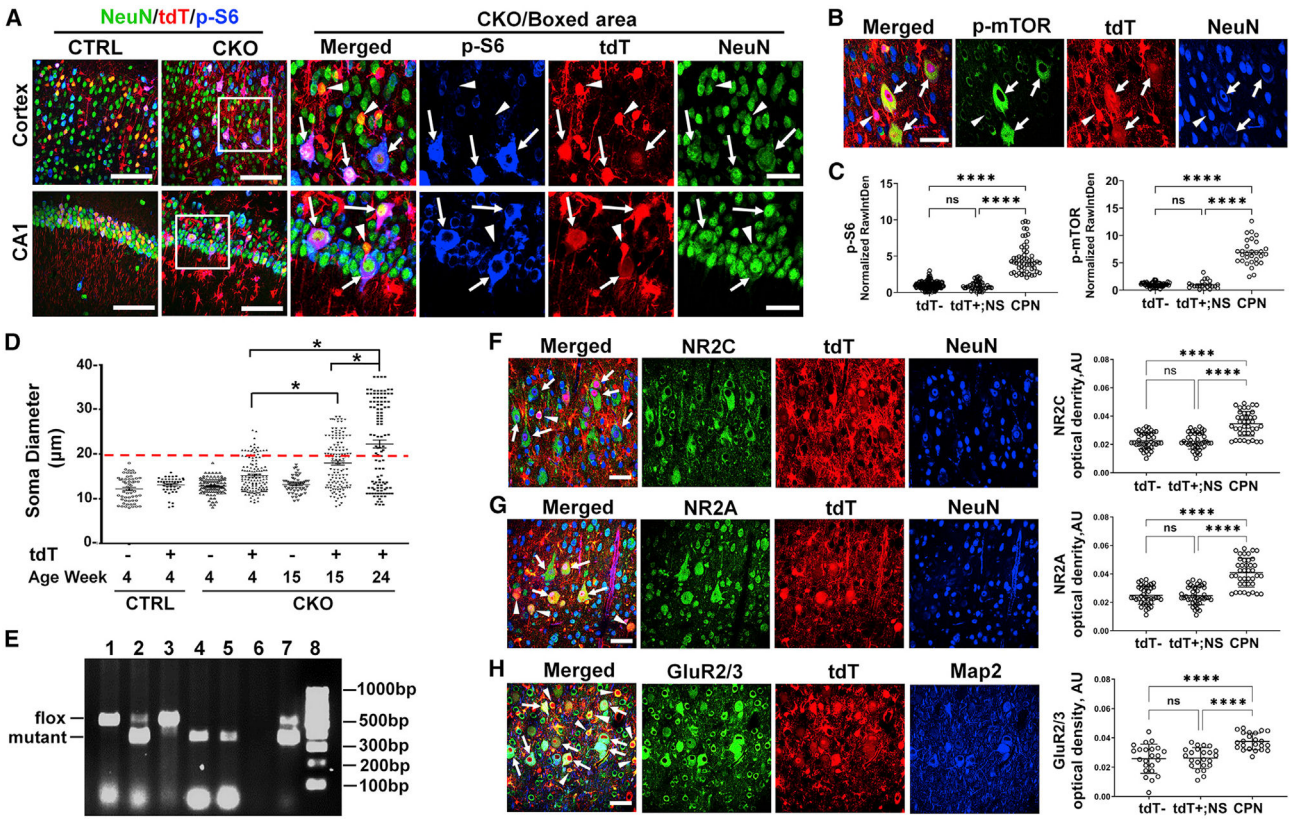

Figure 3. The presence of CPNs in *Tsc1*CKO mice

(A) Immunolabeling of p-S6 in the upper cortex (top) and hippocampal CA1 area (bottom) of *mGfap*-Cre+:Ai9+ CTRL and *Tsc1*CKO:*Ai9+* (CKO) mice at postnatal week 15. CPNs are indicated by arrows, and tdT+ normal-sized (tdT+; NS) pyramidal neurons by arrowheads. Scale bars, 150 μm (left) and 50 μm (right).

(B) Immunolabeling of p-mTOR in the cortex of CKO mice. CPNs are indicated by arrows, and tdT+;NS pyramidal neurons by arrowheads. Scale bar, 50 μm.

(C) Quantification of p-S6 (left) and p-mTOR (right) in CPNs and adjacent upper cortical tdT− and tdT+;NS pyramidal neurons in CKO mice.

(D) Somal size of tdT+ neurons in CKO mice with age. The dotted line sets a cutoff value (20 μm) for the separation of CPNs (above) from tdT− and tdT+;NS pyramidal neurons (below).

(E) Genotyping of *Tsc1* flox (~486 bp) and null (~368 bp) alleles in different neuronal types in CKO mice. After electrophysiological characterization, the nucleus from each neuron is aspirated through a patch-clamp pipette. Approximately 50 nuclei from the same neuronal type are pooled for genotyping. Lane 1: upper cortex from $Tsc1^{flox/flox}$ mice, showing one single band for the *Tsc1* flox allele. Lanes 2 and 7: upper cortex from *CKO* mice, showing a lower band for the *Tsc1*-null allele and a weak upper band for the flox allele that is derived from non-recombinant cells. Lanes 3–5: tdT− pyramidal neurons (lane 3), tdT+;NS pyramidal neurons (lane 4), and tdT+ cytomegalic neurons (lane 5) from the upper cortex of CKO mice. Lane 6: DNA sample without primers. Lane 8: DNA ladder.

(F–H) CPNs (arrows) express higher levels of NR2C (F), NR2A (G), and GluR2/3 (H) than adjacent tdT+;NS (arrowhead) and tdT− pyramidal neurons. Scale bars, 50 μm.
For each genotype, 4–5 mice are used at each age. ns, non-significant; *$p < 0.05$, **$p < 0.01$, ***$p < 0.001$, ****$p < 0.0001$. One-way ANOVA in (C), (D), and (F)–(H).

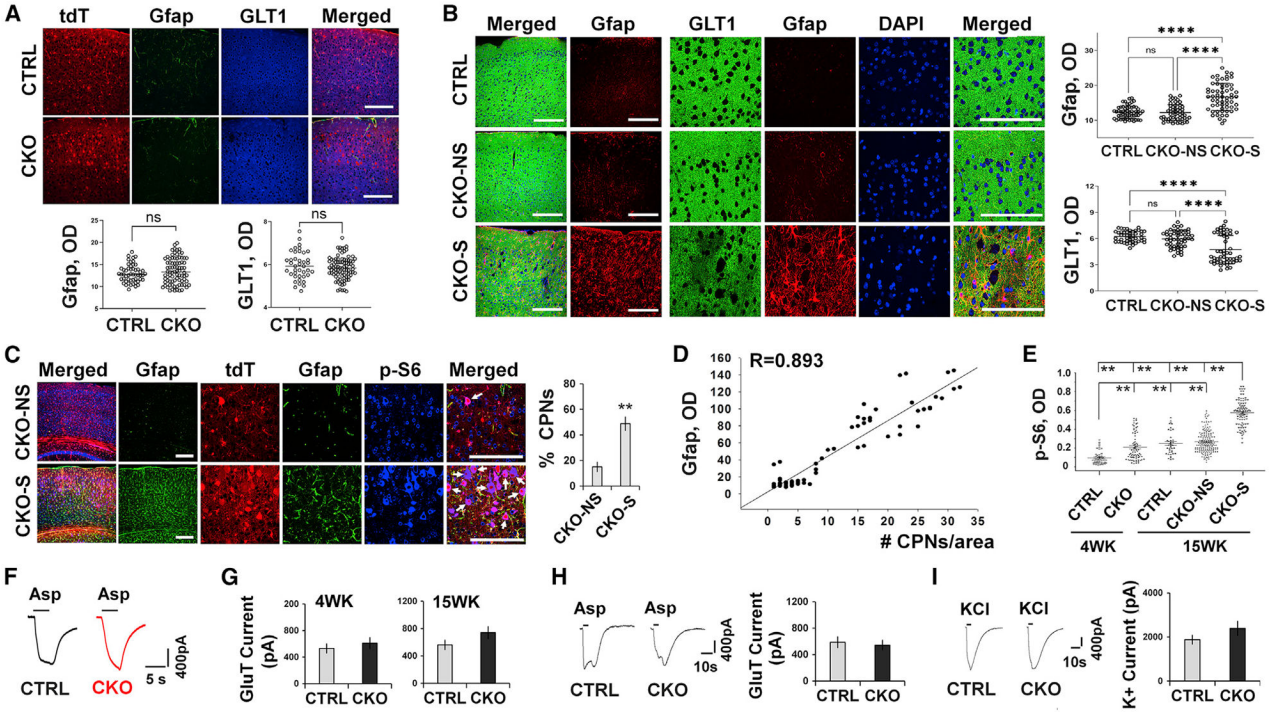

Figure 4. Lack of astrogliosis and astrocyte dysfunction in *Tsc1*CKO mice without seizures

(A) Immunolabeling for Gfap and GLT1 in the cortex of *mGfap*-Cre; Ai9+ (CTRL) and *Tsc1*CKO:Ai9+ (CKO) mice at postnatal week 4. Scale bars, 200 μm. The dot plots show Gfap or GLT1 optical density (OD) per astrocyte, measured in arbitrary units (a.u.). There are no significant differences between groups (unpaired t test) despite a very few astrocytes from CKO mice showing higher levels of Gfap than all astrocytes from CTRL mice.

(B) Immunolabeling for Gfap and GLT1 in the cortex of CTRL and CKO mice after postnatal week 15. CKO-S, CKO mice with seizures; CKO-NS, CKO mice without seizures. Gfap and GLT1 levels of individual astrocytes are quantified. ****$p < 0.001$, one-way ANOVA. Scale bars, 200 μm.

(C) Immunolabeling for Gfap and p-S6 in CKO-S and CKO-NS mice after postnatal week 15. CPNs (arrows) are distinguished by their expression of tdT, enlarged pyramid-shaped cell bodies, and high levels of p-S6. Scale bars, 200 μm. The bar graph shows the percentage of total tdT+ neurons that are CPNs in CKO-NS (n = 3, ~15.0%) and CKO-S (n = 3, ~50.6%) mice.

(D) Correlation between the number of CPNs and the level of Gfap in CKO mice. Gfap OD is plotted against the number of CPNs per imaging area (295 × 295 μm).

(E) Astrocyte p-S6 levels in CTRL, CKO-S, or CKO-NS mice. Each dot represents p-S6 OD of a single astrocyte. At postnatal week 4, a few *Tsc1*KO astrocytes show increased p-S6 levels. At postnatal week 15, astrocyte p-S6 levels are similar between CTRL and CKO-NS mice, whereas the majority of astrocytes in CKO-S mice show elevated pS6 levels. **$p < 0.01$, one-way ANOVA. 4–5 mice are used per condition.

(F) Representative traces for glutamate transporter (GLUT)-mediated current in cortical astrocytes from CTRL and CKO-NS mice at postnatal week 15.

(G) Cortical astrocyte GLUT current at postnatal weeks 8 and 15 in CKO-NS mice, indicating normal astrocyte glutamate uptake at both ages.
(H and I) Hippocampal astrocyte glutamate uptake (H) and potassium buffering (I) are comparable between CTRL and CKO-NS mice at postnatal week 15. At each age, 6–8 tdT+ astrocytes are recorded from 3–4 mice per genotype.

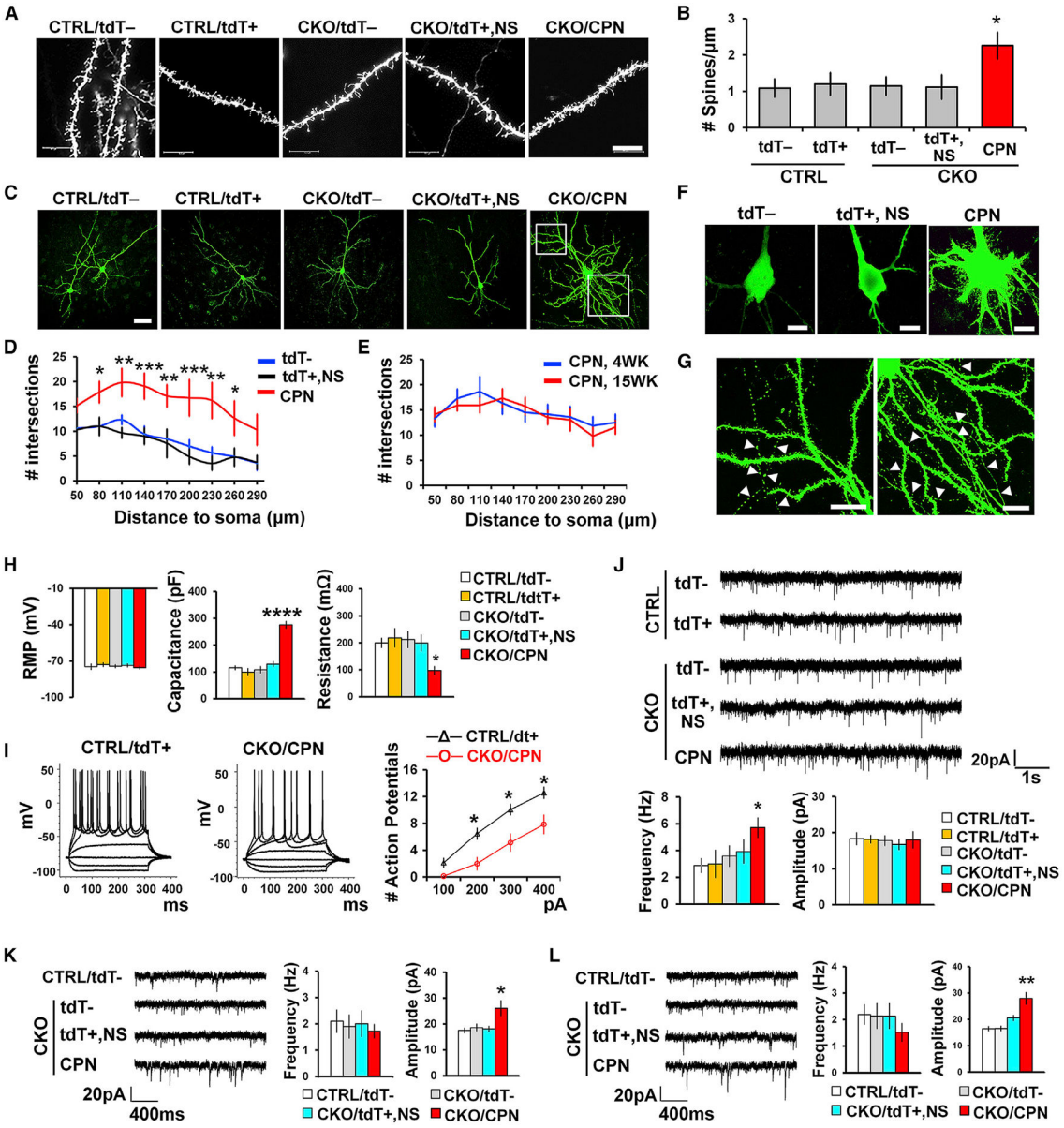

Figure 5. Glutamatergic synapses are strengthened in CPNs

(A–I) CTRL/tdT− and CTRL/tdT+, tdT− or tdT+ layer 2/3 upper cortical pyramidal neurons from *mGfap-Cre;Ai9+* (CTRL) mice; CKO/tdT−, tdT− layer 2/3 upper cortical pyramidal neurons from *Tsc1CKO:Ai9+* (CKO) mice; CKO/tdT+,NS, tdT+ normal sized (NS) *Tsc1*KO pyramidal neurons from the upper cortex of CKO mice; CKO/CPN, CPNs in the upper cortex of CKO mice.

(A) Representative images of basal dendrites from DiO ($DiO_{18}(3)$) -labeled upper cortical pyramidal neurons at postnatal week 4. Scale bar, 10 μm.

(B) Quantification of dendritic spine density. Mature spines were defined as dendritic protrusions with a ratio of head/neck diameter greater than 1.1 (Tang et al., 2014). Three dendritic segments per neuron, 12–15 neurons from 3–4 mice per condition.

(C) Representative images of Lucifer yellow-filled upper cortical pyramidal neurons. Scale bar, 50 μm. Boxed regions are shown in (G).
(D) Sholl analysis of dendritic arborization in CKO mice at postnatal week 4. Compared with tdT− *Tsc1*WT and tdT+ NS *Tsc1*KO neurons, CPNs show increased numbers of intersections at all distances from the soma. n = 7–9 neurons from 3–4 mice per condition.
(E) In CKO mice, CPNs show comparable dendritic arborization at postnatal weeks 4 and 15.
(F) CPNs exhibit exuberant thin processes in the somatodendritic domain compared with adjacent tdT− and tdT+ NS neurons. Scale bar, 10 μm.
(G) CPNs show recurrent axon collaterals (arrowheads) projecting into their own dendrites. Scale bar, 20 μm.
(H) Compared with other neuronal types, CPNs show an increase in membrane capacitance, a reduction in membrane input resistance, but no changes in resting membrane potential (RMP).
(I) Compared with CTRL/tdT+ neurons, CPNs show a reduction in AP firing in response to current injections.
(J) At postnatal week 4, CPNs show an increase in sEPSC frequency over other neuronal types.
(K and L) CPNs show increased sEPSC amplitude over other neuronal types at postnatal weeks 8 (K) and 15 (L).
For each neuronal type, 7–16 neurons are recorded from 5–6 mice per genotype at each age. Compared with CTRL/tdT+ neurons, *$p < 0.05$, **$p < 0.01$, ****$p < 0.0001$. One-way ANOVA for (B), (H), and (J)–(L); two-way ANOVA for (D) and (I).

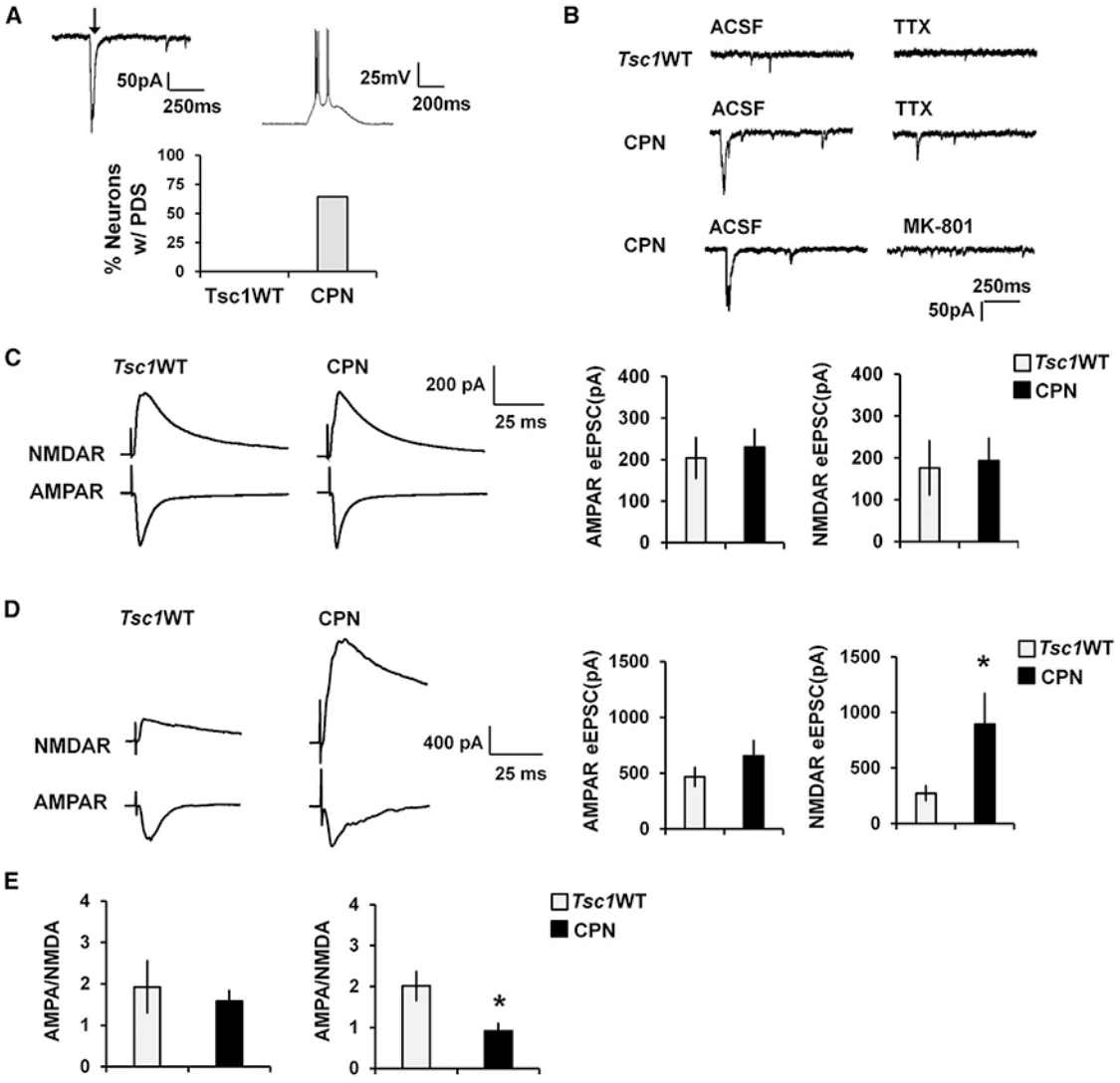

Figure 6. NMDAR-mediated glutamate synaptic transmission is enhanced in CPNs after postnatal week 8

(A–E) *Tsc1*WT, tdT+ layer 2/3 upper cortical pyramidal neurons from *mGfap-Cre:Ai9+* (CTRL) mice; CPN, CPNs in the upper C of *Tsc1*CKO:Ai9+ mice.

(A) After postnatal week 8, CPNs show PDS-like giant inward currents (arrow) recorded in voltage-clamp mode (top left) and spiking events recorded in current-clamp mode (top right). The bar graph shows the percentage of CPNs (9 of 14) and *Tsc1*WT neurons (0 of 33) with PDS-like events.

(B) Giant inward currents in CPNs can be abolished by tetrodotoxin (TTX; 1 μM) or the NMDAR blocker MK-801 (10 μM).

(C) At postnatal week 4, CPNs and *Tsc1*WT neurons show similar NMDA– and AMPA–EPSCs. An NMDA-dependent EPSC is measured at +40 mV, 50 ms from the stimulus artifact.

(D) After postnatal week 8, CPNs show significantly higher NMDA– EPSCs than *Tsc1*WT neurons.

(E) AMPA:NMDA ratio in *Tsc1*WT neurons and CPNs at postnatal week 4 (left) and after postnatal week 8 (right). *$p < 0.05$, unpaired t test. n = 5–6 neurons for each neuronal type.

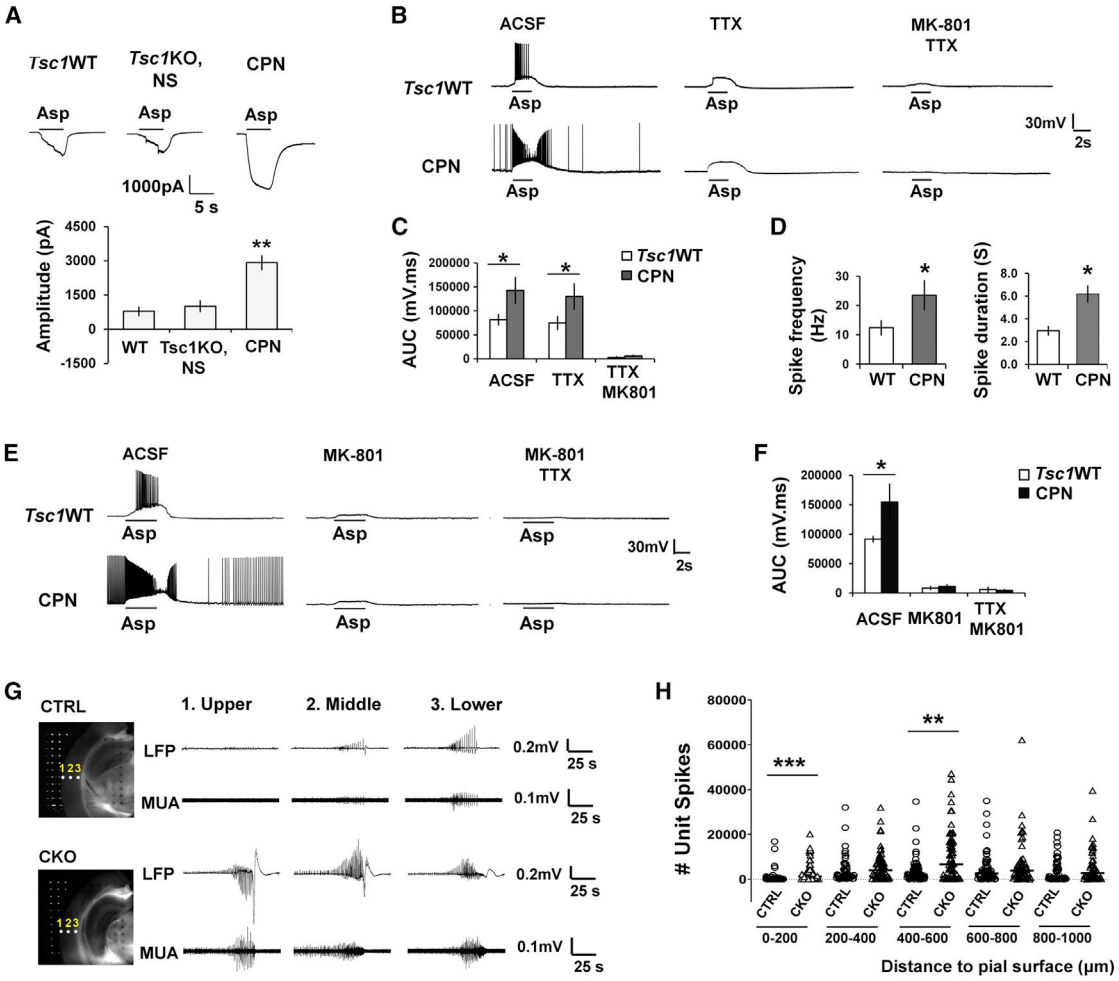

Figure 7. CPNs are more susceptible to seizure-like activities after postnatal week 8

(A–H) *Tsc1*WT, tdT+ layer 2/3 upper cortical pyramidal neurons from *mGfap-Cre:Ai9+* (CTRL) mice; CPN, CPNs in the upper cortex of *Tsc1*CKO:Ai9+ mice.

(A) Giant inward current induced by D-aspartic acid (Asp; 1 mM) in the presence of TTX (1 μM). CPNs, n = 8; *Tsc1*WT, n = 9; normal-sized *Tsc1*KO neurons (*Tsc1*KO, NS), n = 8. Compared with *Tsc1*WT, **p < 0.01; one-way ANOVA.

(B) Typical Asp-induced traces in current-clamp mode from *Tsc1*WT neurons (n = 5) and CPNs (n = 5) recorded after 5 min in TTX (1 μM, center) and 5 min in TTX/MK-801(10 μM, right).

(C) Membrane depolarization measured by the area under the curve (AUC). Compared with *Tsc1*WT neurons (n = 5), CPNs (n = 5) show greater depolarization. TTX has no effect on membrane depolarization in *Tsc1*WT neurons and CPNs. *p < 0.05, two-way ANOVA.

(D) Quantification of Asp-induced spikes riding on top of the membrane depolarization. Compared with *Tsc1*WT neurons (n = 10), all CPNs (10 of 10) show increased firing frequency and duration in response to Asp. *p < 0.05, unpaired t test. Prior to application of Asp, 30% (3 of 10) of CPNs but no (0 of 10) *Tsc1*WT neurons present spontaneous spiking activities.

(E) MK-801 (10 μM, 5 min) blocks Asp-induced membrane depolarization and spike firing in all *Tsc1*WT neurons (5 of 5) and CPNs (5 of 5). Neurons are treated with MK-801 (center) prior to application of TTX (right).

(F) Quantification of Asp-induced membrane depolarization from (E). *$p < 0.05$, two-way ANOVA.

(G) MEA analysis of CTRL and CKO cortices bathed in Mg^{2+}-free ACSF. Left: the positions of microelectrodes. Right: representative traces of multi-unit activity (MUA) and local field potentials (LFPs) recorded from the upper (electrode 1), middle (electrode 2), and lower (electrode 3) C.

(H) Comparison of unit spiking activities between CTRL and CKO slices across different cortical depths. The number of unit spikes is derived from MUA recorded from each microelectrode during the recording period. **$p < 0.01$, ***$p < 0.001$. Kruskal-Wallis test followed by Tukey's multiple comparisons. For each genotype, N = 6–8 slices from 45 mice.

KEY RESOURCES TABLE

REAGENT or RESOURCE	SOURCE	IDENTIFIER
Antibodies		
Mouse anti-Map2	Sigma Aldrich	Cat# M9942; RRID:AB_477256
Rabbit anti-Map2	Millipore	Cat# AB5622; RRID:AB_91939
Mouse Anti-Neurofilament	Covance	Cat# SMI-311; RRID:AB_2315332
Mouse anti-NeuN	Millipore	Cat# MAB377; RRID:AB_2298772
Mouse anti- Tubulin β3	BioLegend	Cat# 801201; RRID:AB_2313773
Rabbit anti-NR2A	Millipore	Cat# 07-632; RRID:AB_310837
Goat anti- NMDAepsilon2	Santa Cruz Biotechnology	Cat# sc-1469; RRID:AB_670229
Goat anti- NMDAepsilon3	Santa Cruz Biotechnology	Cat# sc-1470; RRID:AB_670233
Rabbit anti-GluR2/3	Millipore	Cat# AB1506; RRID:AB_90710
Mouse anti-GFAP	Sigma-Aldrich	Cat# G3893; RRID:AB_477010
Rabbit anti-GFAP	Agilent	Cat# Z0334; RRID:AB_10013382
Mouse anti- EAAT1/GLAST	Leica Biosystems	Cat# NCL-EAAT1; RRID:AB_564088
Mouse anti-EAAT2/GLT1	BD Biosciences	Cat# 611654; RRID:AB_399172
Rabbit anti-S100β	Agilent	Cat# Z031129-2; RRID:AB_2315306
Rabbit anti-Nestin	Sigma-Aldrich	Cat# N5413; RRID:AB_1841032
Goat anti-Vimentin	Santa Cruz Biotechnology	Cat# sc-7557; RRID:AB_793998
Rabbit anti-phospho-mTOR	Cell Signaling Technology	Cat# 2976; RRID:AB_490932
Rabbit anti- phospho-S6	Cell Signaling Technology	Cat# 5364; RRID:AB_10694233
Rabbit anti-Lucifer Yellow	Sigma-Aldrich	Cat# L9163; RRID:AB_260435
Rabbit anti-Cux1/CDP	Santa Cruz Biotechnology	Cat# sc-13024; RRID:AB_2261231
Rabbit anti-Foxp2	Abcam	Cat# ab16046; RRID:AB_2107107
Rat anti-Ctip2	Abcam	Cat# ab18465; RRID:AB_2064130
Guinea Pig anti-ZnT3	Synaptic Systems	Cat# 197 004; RRID:AB_2189667
Mouse anti-GAD-65/67	Santa Cruz Biotechnology	Cat# sc-365180; RRID:AB_10710523
Rabbit anti-Parvalbumin	Novus Biologicals	Cat# NB120-11427; RRID:AB_791498
Rabbit anti-GABA	Sigma-Aldrich	Cat# A2052; RRID:AB_477652
Alexa 488 Conjugated Donkey Anti-Mouse IgG (H+L)	ThermoFisher Scientific	Cat# A21202; RRID:AB_141607
Alexa 488 Conjugated Donkey Anti-Rabbit IgG (H+L)	ThermoFisher Scientific	Cat# A32790; RRID:AB_2762833
Alexa 488 Conjugated Donkey Anti-goat IgG (H+L)	ThermoFisher Scientific	Cat# A32814; RRID:AB_2762838
Alexa 594 Conjugated Donkey Anti-Mouse IgG (H+L)	ThermoFisher Scientific	Cat# A32744; RRID:AB_2762826
Alexa 594 Conjugated Donkey Anti-Rabbit IgG (H+L)	ThermoFisher Scientific	Cat# R37119; RRID:AB_2556547
Alexa 594 Conjugated Donkey Anti-goat IgG (H+L)	ThermoFisher Scientific	Cat# A32758; RRID:AB_2762828
Alexa 647 Conjugated Donkey Anti-Mouse IgG (H+L)	ThermoFisher Scientific	Cat# A32787; RRID:AB_2762830
Alexa 647 Conjugated Donkey Anti-Rabbit IgG (H+L)	ThermoFisher Scientific	Cat# A-31573; RRID:AB_2536183
Alexa 647 Conjugated Donkey Anti-goat IgG (H+L)	ThermoFisher Scientific	Cat# A32849; RRID:AB_2762840
Alexa 594 conjugated Donkey anti Rat IgG	ThermoFisher Scientific	Cat# A-21209; RRID:AB_2535795
Rabbit anti-Phospho mTOR (Ser2448)	Cell Signaling Technology	Cat# 2971; RRID:AB_330970
Rabbit anti-mTOR	Cell Signaling Technology	Cat# 2972; RRID:AB_330978
Rabbit anti-Phospho-S6	Cell Signaling Technology	Cat# 2211; RRID:AB_331679

REAGENT or RESOURCE	SOURCE	IDENTIFIER
Mouse anti-S6	Cell Signaling Technology	Cat# 2317; RRID:AB_2238583
Mouse anti-Actin	Sigma-Aldrich	Cat# A5441; RRID:AB_476744
Mouse anti-TSC1	Millipore	Cat# 05-1113; RRID:AB_11214491
Rabbit anti-Kir4.1	Millipore	Cat# AB5818; RRID:AB_92052
Guinea Pig anti-GLT1	Millipore	Cat# AB1783; RRID:AB_90949
Rabbit anti-EAAT1/GLAST	Santa Cruz Biotechnology	Cat# sc-15316; RRID:AB_2302051
Mouse anti-Thrombospondin 4	Santa Cruz Biotechnology	Cat# sc-390734; RRID:AB_2753205
Mouse anti-Thrombospondin 1/2	Santa Cruz Biotechnology	Cat# sc-133061; RRID:AB_2202075
Mouse anti-MerTK	Santa Cruz Biotechnology	Cat# sc-365499; RRID:AB_10843860
Rabbit anti-GPC4	Proteintech	Cat# 13048-1-AP; RRID:AB_10640157
Goat anti-SPACL1/Hevin	R and D Systems	Cat# AF2836; RRID:AB_2195097
Rabbit anti-Aquaporin	Abcam	Cat# ab46182; RRID:AB_955676
Mouse anti-Vimentin	Agilent	Cat# M0725; RRID:AB_10015203
Peroxidase-AffiniPure Donkey Anti-Goat IgG (H+L)	Jackson ImmunoResearch Labs	Cat# 705-035-147; RRID:AB_2313587
Peroxidase-AffiniPure Donkey Anti-Mouse IgG (H+L)	Jackson ImmunoResearch Labs	Cat# 715-035-151; RRID:AB_2340771
Peroxidase-AffiniPure Donkey Anti-Guinea Pig IgG (H+L)	Jackson ImmunoResearch Labs	Cat# 706-035-148; RRID:AB_2340447
Peroxidase-AffiniPure Donkey Anti-Rabbit IgG (H+L)	Jackson ImmunoResearch Labs	Cat# 711-035-152; RRID:AB_10015282
Peroxidase-AffiniPure Donkey Anti-Rat IgG (H+L)	Jackson ImmunoResearch Labs	Cat# 712-035-153; RRID:AB_2340639
Chemicals, peptides, and recombinant proteins		
Tamoxifen	Sigma	Cat# T5648; CAS:10540-29-1
Corn oil	Sigma	Cat# C8267; CAS: 8001-30-7
Restore™ Western Blot Stripping Buffer	Thermofisher Scientific	Cat# 21063
Blotting-Grade Blocker	Biorad	Cat# 1706404
Bio-Rad Protein Assay Dye Reagent Concentrate	Biorad	Cat# 5000006
20X Tris Buffered Saline	Santa Cruz Biotechnology	Cat# sc-362305
D-aspartic acid	Sigma	Cat# 219096; CAS: 1783-96-6
MK-801	Tocris	Cat# 0924; CAS: 77086-22-7
NBQX	Tocris	Cat# 1044; CAS: 479347-86-9
Lucifer yellow	Sigma	Cat# L-0259
Tetrodotoxin	Tocris	Cat# 1069; CAS: 18660-81-6
D-AP5	Tocris	Cat# 0106; CAS: 79055-68-8
Picrotoxin	Tocris	Cat# 1128; CAS: 124-87-8
TBOA	Tocris	Cat# 1223; CAS: 205309-81-5
DiO	Thermofisher Scientific	Cat# D-275
Critical commercial assays		
Clarity™ Western ECL Substrate	Biorad	Cat# 1705061
Clarity Max™ Western ECL Substrate	Biorad	Cat# 1705062
Deposited data		
Raw and analyzed data	This paper	GEO: GSE156891
Experimental models: Organisms/strains		
Mouse: *Tsc1*$^{mGfap\text{-}Cre}$CKO:*Ai9+*	This paper	N/A

REAGENT or RESOURCE	SOURCE	IDENTIFIER
Mouse: *Tsc1*$^{hGFAP\text{-}CreER}$CKO:*Ai9+*	This paper	N/A
Mouse: *Tsc1*$^{mGfap\text{-}Cre}$CKO:RiboTag	This paper	N/A
Mouse: *mGfap-Cre;Ai9+*	This paper	N/A
Mouse: *hGFAP-CreER;Ai9+*	This paper	N/A
Mouse: *mGfap*-Cre:Rosa-EYFP+	This paper	N/A
Mouse: *mGfap-Cre*:RiboTag	This paper	N/A
Mouse: *Tsc1*$^{flox/flox}$	Jackson laboratory; Kwiatkowski et al., 2002	RRID: IMSR_JAX: 005680
Mouse: *mGfap-Cre*	Jackson laboratory; Garcia et al. (2004)	RRID: IMSR_JAX: 012,886
Mouse: *hGFAP-CreER*	Jackson laboratory; Ganat et al. (2006)	RRID: IMSR_JAX: 012,849
Mouse: *Ai9*	Jackson laboratory; Madisen et al., 2010	RRID: IMSR_JAX: 007909
Mouse: Rosa-EYFP	Jackson laboratory; Srinivas et al. (2001)	RRID: IMSR_JAX: 006148
Mouse: RiboTag	Jackson laboratory; Sanz et al. (2009)	RRID: IMSR_JAX: 029977
Software and algorithms		
R	R foundation	N/A
GraphPad Prism	GraphPad	RRID:SCR_002798
pClamp	Molecular Devices	RRID:SCR_011323
Image J	NIH	RRID:SCR_003070
Imaris/FilamentTracer	Bitplane	RRID:SCR_007366
Mini Analysis Program	SynaptoSoft	RRID:SCR_002184
TopHat	http://ccb.jhu.edu/software/tophat	RRID:SCR_013035
DEseq2	Bioconductor	RRID:SCR_015687
bcl2fastq Conversion Software v1.8.4	Illumina	N/A
Real-Time Analysis (RTA)	Illumina	N/A
Blackrock offline spike sorter	Blackrock microsystems	N/A
any-maze video tracking software	Stoelting Co.	N/A
Observer XT	Noldus Information Technology	N/A
Ethovision XT	Noldus Information Technology	RRID:SCR 000441